

Medical Imaging Synthesis using Deep Learning and its Clinical Applications: A Review

Tonghe Wang^{1,2}, Yang Lei¹, Yabo Fu¹, Walter J. Curran^{1,2}, Tian Liu^{1,2} and Xiaofeng Yang^{1,2*}

¹Department of Radiation Oncology, Emory University, Atlanta, GA

²Winship Cancer Institute, Emory University, Atlanta, GA

***Corresponding author:**

Xiaofeng Yang, PhD

Department of Radiation Oncology

Emory University School of Medicine

1365 Clifton Road NE

Atlanta, GA 30322

E-mail: xiaofeng.yang@emory.edu

Abstract

This paper reviewed the deep learning-based studies for medical imaging synthesis and its clinical application. Specifically, we summarized the recent developments of deep learning-based methods in inter- and intra-modality image synthesis by listing and highlighting the proposed methods, study designs and reported performances with related clinical applications on representative studies. The challenges among the reviewed studies were summarized in the discussion part.

1 INTRODUCTION

Image synthesis between different medical imaging modalities/protocols is an active research field with great clinical interest in radiation oncology and radiology. It aims to facilitate a specific clinical workflow by bypassing or replacing a certain imaging procedure when the acquisition is infeasible, costs additional time/labor/expense, has ionizing radiation exposure, or introduces uncertainty from image registration between different modalities. The proposed benefit has raised increasing interest in a number of potential clinical applications such as magnetic resonance imaging (MRI)-only radiation therapy treatment planning, positron emission tomography (PET)/MRI scanning, and etc.

Image synthesis with its potential applications has been investigated for decades. The conventional methods usually rely on models with explicit human-defined rules about the conversion of images from one modality to the other. These models are usually application-specific depending on the unique characteristics of the involved pair of imaging modalities, thus can be diverse in methodologies and complexities. It is also hard to build such a model when the two imaging modalities provide distinct information, such as anatomic imaging and functional imaging. This is partially why the majority of these studies are limited to image synthesis between computed tomography (CT) images from MRI.[64] These methods usually require case-by-case parameters tuning for optimal performance.

Owing to the widespread success of machine learning in computer vision field in recent years, the latest breakthrough in artificial intelligence has been integrated into medical image synthesis. In addition to CT-MRI synthesis, image synthesis in other imaging modalities such as PET and cone-beam CT (CBCT) is now viable. As a result, more and more applications could benefit from the recent advancements of image synthesis techniques.[155, 156, 174] Deep learning, as a large subset of machine learning and artificial intelligence, is dominating in this field in the past several years. Deep learning utilizes neural network with many layers containing huge number of neurons to extract useful features from images. Various networks and architectures have been proposed for better performance on different tasks. Deep learning-based image synthesis methods usually share a common framework that uses a data-driven approach for image intensity mapping. The workflow usually consists of a training stage for the network to learn the mapping between the input and its target, and a prediction stage to synthesize the target from an input. Compared with conventional model-based methods, deep learning-based methods are more generalizable since the same network and architecture for a pair of image modalities can be applied to different pairs of image modalities with minimal adjustment. This allows rapid expansion of applications using a similar methodology to a variety of imaging modalities that are clinically desired for image synthesis. The performance of the deep learning-based methods largely depends on the representativeness of the training datasets rather than case-specific parameters. Although the network training may require lots of efforts in collecting and cleaning training datasets, the prediction usually takes only a few seconds. Due to these advantages, deep learning-based methods have attracted great research and clinical interest in medical imaging and radiation therapy.

In this paper, we systematically reviewed the emerging deep learning-based methods and applications for medical image synthesis. Specifically, we categorized the recent literatures based on their deep learning properties and highlighted their contributions. The clinical scenario of applications was then summarized with challenges and concerns identified. The trend and future direction on this topic were discussed in the end of this review.

2 LITERATURE SEARCHING

We defined the scope of this review study to include both inter-modality and intra-modality image synthesis using deep learning method. Inter-modality applications included studies about the image synthesis between two different imaging modalities. Intra-modality applications included studies that transform images between two different protocols of a same imaging modality, such as between different MR imaging sequences, or the restoration of images from low quality protocol to high quality protocol. Studies solely aiming for image quality improvement such as image denoising and artifact correction were not included in this study. Conference abstracts and proceedings were not considered due to the lack of strict peer review process in study design and reported results.

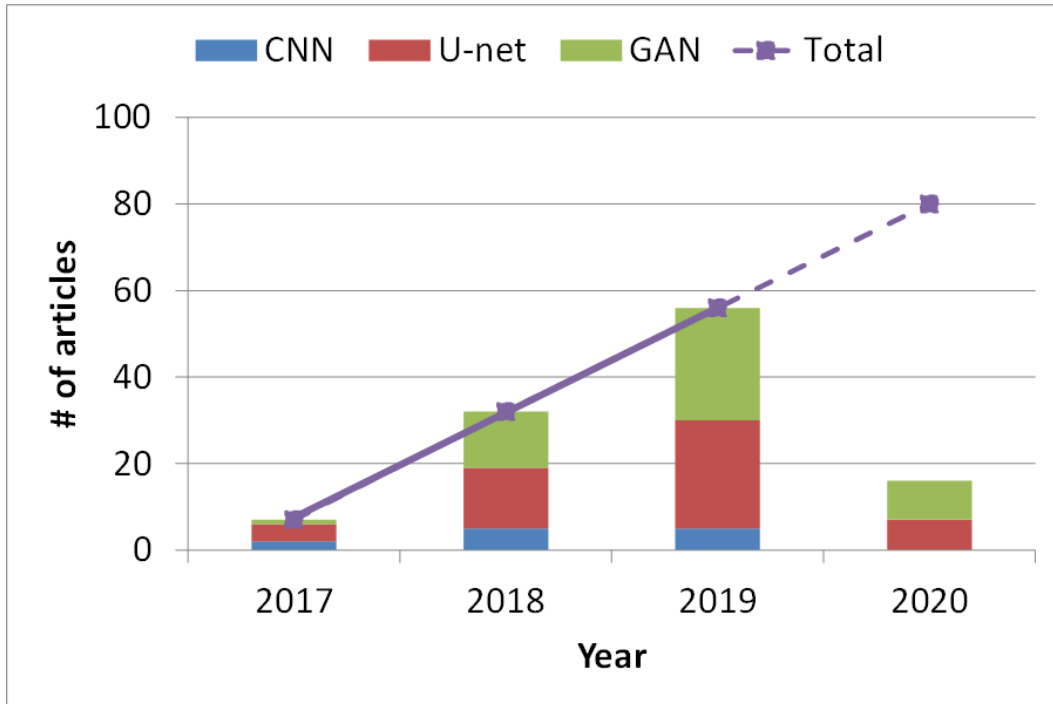


Figure 1. Number of peer-reviewed articles in medical imaging synthesis using deep learning with different neural networks. This study only covers the first two month of 2020. The dashed line predicting the total number of articles in 2020 is a linear extrapolation based on previous years.

Peer-reviewed journal publications were searched on PubMed using the criteria in title or abstract as of February 2020 : (pseudo OR synth* OR reconstruct* OR transform OR restor* OR correct* OR generat*) AND deep AND learning AND (CT OR MR OR MRI OR PET OR SPECT OR Ultrasound). The search yielded 681 records. We manually screened each record and removed ineligible ones, and the remaining 70 articles were included in this review study. We also performed a citation search on the identified literatures, and additional 41 articles were included. Therefore, 111 articles in total were included in this review. Compared with current review papers on this topic,[177] this review study is comprehensive in covering more articles by a systematic review approach. Figure 1 shows the number of reviewed articles in each year. With the earliest one published in 2017 and an increment of about 25 per year, the number of publications on this topic has increased linearly. The number of articles in the first two months of 2020 has surpassed the total number in 2017.

3 DEEP LEARNING METHODS

The framework of the reviewed studies can be grouped into three categories: Convolutional Neural Network (CNN), U-net, and Generative Adversarial Network (GAN). The pie chart of the three groups shown in Figure 2 indicates that U-net and GAN studies, which are close in total numbers, are the mainstream that accounts for about 90%. Figure 1 also demonstrates that the studies using U-net and GAN keep increasing since 2017, with GAN in a larger rate than U-net. Most methods of all these three categories are supervised learning. Three out of 111 studies used an unsupervised strategy that learned image translation from unpaired datasets. The three categories, CNN, U-net and GAN, have an increasing complexity and are not completely distinct from each other. A review of methods in each category is provided in this section.

3.1 Convolutional Neural Network

Convolutional Neural Network (CNN) is a class of deep neural networks that use convolution kernels to explore the spatially local image patterns. It consists of an input, an output, and multiple hidden

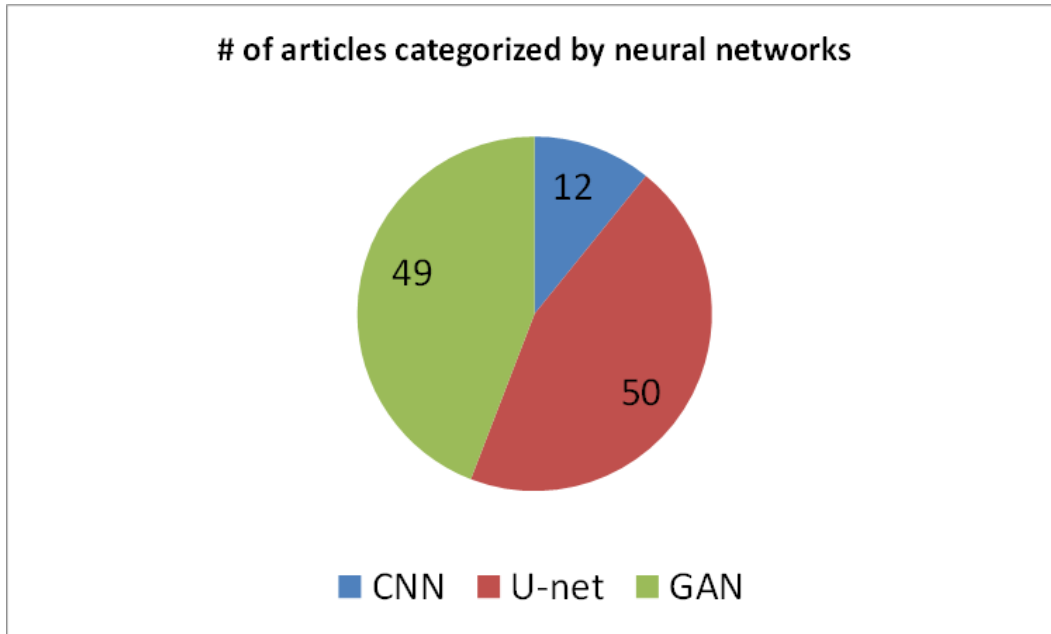


Figure 2. Pie chart of numbers of articles in different categories of neural networks.

layers. The hidden layers contain a series of convolutional layers that convolve the input with trainable convolution kernels and pass the feature maps to the next layer. Rectified linear unit (ReLU) layer is the commonly used activation layer due to its computational simplicity, representational sparsity and linearity. Dropout layers are commonly used to reduce chances of overfitting. Batch normalization layer is usually employed to reduce internal covariate shift of the training datasets for improved robustness and faster convergency. To save memory, the large size of image is typically reduced after pooling and convolution layers to allow larger number of feature maps and deeper networks. With multiple hidden convolutional layers, a hierarchy of increasingly complex features with high-level abstraction is then extracted. During the training process, iterative adjustments are made on the weights and biases of the kernels of these convolutional layers until the loss function is minimized. These weights and biases are called trainable parameters of networks. Gradient descent methods, such as Adam optimizer, are used to update trainable parameters of our networks. A simple basic CNN is composed of several connected convolutional layers to map input to output. Nonetheless, very few studies directly employ CNN in its basic form. Most of the reviewed studies used variants of basic CNN for better performance. For example, ResNet was chosen in a few studies since it has short-cut connections for each block that skip one or more layers, which eases the training of the deep network without adding extra parameters or computational complexity.[30, 117, 146] It also allows feature maps from the initial layers that usually contain fine details to be easily propagated to the deeper layers. CNN and its variants are commonly utilized as a basic component in advanced architectures such as the ones listed in the following.

3.2 U-net

As one of the first several studies employing deep learning in image synthesis, Han used CNN in synthesizing CT from MR images by adopting and modifying a U-net architecture.[42] The U-net model used in the study of Han has an encoding and a decoding part. The encoding part acts as the CNN mentioned above that extract hierarchical features from an input MR image with convolutional, batch normalization, ReLU and pooling layers, and the decoding part, a mirrored version of the encoding part that replaces pooling layers with deconvolution layers, transforms the features and reconstructs the predicted CT images from low to high resolution levels. The two parts are connected through short-cuts on multiple layers such that high-resolution features from encoding part can be used as extra inputs in the decoding part. Moreover, the model removed fully-connected layers such that the number of parameters was highly reduced. In their study, the model was trained by pairs of MR and CT 2D slices. During the learning process, a loss function of mean absolute error (MAE) between prediction and ground truth was minimized. The usage of this L1-norm as loss function can help the learning be more robust to noise, artifacts and misalignment among the training images.

Most of the studies applying U-net into their model generally followed the above architecture, with many variants and improvements proposed and studied. For example, compared with the model of Han, Liu *et al.* applied a similar encoder and decoder model while without the skip connection.[56, 100] In their MR-based sCT study, instead of using CT images as training and prediction target, they used discretized maps from CTs by labeling three materials, which converted the CT synthesis into a segmentation problem. Thus, a multi-class soft-max classifier was added on the final layer of the decoder to produce class probabilities for each voxel. Another difference in Ref. [56] is that since this model was based on 2D image slices, a fully connected conditional random field was added to consider the 3D contextual relationship between voxels since it can take the output of the model and take the original 3D volume to build the pairwise potentials on all pairs of voxels. Dong *et al.* found that the information that the long skip connection in U-net concatenates from the encoding path is high frequency, which often includes irrelevant components from noisy input images. In order to address this issue, they used a self-attention strategy that uses the feature maps extracted from coarse scale to eliminate noisy responses prior to the concatenation. This self-attention U-net is able to highlight the most salient features from the coding path.[27] Hwang *et al.* also noticed the noise propagation from high frequency feature, thus they only used the contracting path in deeper layers.[53]

The choice of building blocks has also been investigated. Fu *et al.* made a few improvements based on the architecture of Han. For example, batch normalization layers were replaced with instance normalization layers for a better performance when trained with small batch size. The unpooling layers, which produce sparse feature maps, were also replaced with deconvolutional layers that produce dense feature maps. The skip connections were replaced with residual short-cuts, which was inspired by ResNet, to further save computational memory. [34] The ReLU layer was also replaced to be a generalized parametric ReLU (PReLU) in the study of Neppel *et al.* to adaptively adjust the activation function.[118] Torrado-Carvajal *et al.* added a dropout layer before the first transposed convolution of the decoder to avoid overfitting.[147]

Various loss functions have been investigated in the reviewed studies. In addition to the most commonly used L1-norm and L2-norm functions that enforce voxel-wise similarity, other functions that describe different image properties are usually combined into the total loss function. For example, Leynes *et al.* used a total loss function which was a sum of MAE loss, gradient difference loss and Laplacian difference loss, the last two of which help improve image sharpness.[95] Similarly, Chen *et al.* combines the MAE loss with structure dissimilarity loss to encourage whole-structure-wise similarity.[17] L2 regularization has also been incorporated into the loss function in a few studies to avoid overfitting.[143, 144] Kazemifar *et al.* used mutual information, which has been widely used in image registration, in their loss function, and demonstrated its advantages over MAE loss in better compensating the misalignment between CT and MR images. Largent *et al.* introduced a perceptual loss which can mimic human visual perception using similar features rather than only intensities, into their U-net. The perceptual loss was proposed to implement in three different ways with increasing complexity: on a single convolutional layer, on multiple layers with uniform weights, and on multiple layers with different weights that give more importance to the layers yielding the lower MAE.[84]

3.3 Generative Adversarial Network

Generative Adversarial Network (GAN) is composed of a generative network and a discriminative network that are trained simultaneously. The generative network is trained to generate synthetic images, and the discriminative network is trained to classify an input image as real or synthetic. The training goal of GAN is to let the generative network produce synthetic images as realistic as possible to fool the discriminator, while let the discriminative network to distinguish the synthetic images from real images. In this way, blurry synthetic images can be easily identified by the discriminator since they look considerably fake. This conflict goal explains the name of adversarial. Both networks are trained better and better when they compete against each other until equilibrium is reached. In the prediction stage, the trained generative network is applied on new incoming image.

Similar to CNN, GAN has also been used in one of the earliest publications in medical image synthesis using deep learning. Nie *et al.* used a fully convolutional network (a variant of CNN) and a CNN for the generative and discriminative, respectively.[120] The loss function of the discriminative network was binary cross entropy, which was minimized between its decisions and correct labels. Similarly, in

generative network, a binary cross entropy between the decision by discriminative network and the wrong label for the generated images, was added into the loss function. Since the network in this study was trained in a patch-to-patch manner that may limit the context information available in the training samples, an auto-context model was employed to refine the results.

Based on the basic architecture of GAN, many variants have been designed and investigated. Emami *et al.* adopted conditional GAN (cGAN) in CT synthesis from MR.[30] Unlike unconditional GAN, both the generative and discriminative networks of cGAN observe the input images (e.g. the MR images in CT synthesis from MR). It can be formulated by condition the loss function of discriminator on the input images, which has been proved to be more suitable for image-to-image translation tasks.[1] Liang *et al.* adopted CycleGAN in their CBCT-based synthetic CT study.[98] The CycleGAN includes two generators which are CBCT-CT generator and CT-CBCT generator and two discriminators which are real CT-synthetic CT discriminator and real CBCT-synthetic CBCT discriminator. In the first cycle, the input CBCT is fed into the CBCT-CT generator to synthesize CT, and then the synthetic CT is fed into the CT-CBCT generator to generate cycle CBCT, which is supposed to be same as the input CBCT. The cycle CBCT is compared to the original input CBCT to generate CBCT cycle consistent loss. Meanwhile, the real CT-synthetic CT discriminator distinguishes between the real CT and the synthetic CT to generate CT adversarial loss. To encourage one-to-one mapping between CT and CBCT, a second cycle transformation from CT to CBCT is performed. The second cycle is same as the first cycle, except the roles of CBCT and CT are swapped, i.e. real CT is fed into the same CT-CBCT generator to synthesize CBCT, and then the synthetic CBCT is fed into the same CBCT-CT generator to generate cycle CT. The cycle CT is compared to the real CT to generate CT cycle consistent loss. The real CBCT-synthetic CBCT discriminator distinguishes between the CBCT and the synthetic CBCT to generate CBCT adversarial loss. Unlike GAN, the CycleGAN couples an inverse mapping network by introducing a cycle consistency loss which enhances the network performance, especially when paired training CT/CBCT images are absent. As a result, CycleGAN can tolerate certain level of misalignment in the paired training dataset. This property of CycleGAN is attractive to inter-modality synthesis since misalignment in the training datasets are sometimes inevitable due to the unavailability of exact matching image pairs. In many studies, training images are still paired by registration to preserve quantitative pixel values, remove large geometric mismatch to allow network to focus on mapping details and accelerate training.[45]

Different structures of the feature extraction blocks were found to be useful for different applications. A group of studies showed that CNN with residual blocks can achieve promising results in image transforming tasks where source and target images are largely similar, such as between CT and CBCT, non-attenuation corrected (NAC) PET and attenuation corrected (AC) PET, and low-counting PET and full-counting PET. Since these pairs of images have similar image appearance but are different quantitatively, residual blocks were integrated into the network to learn the differences between the pairs; each residual block includes a residual connection and multiple hidden layers. An input bypasses these hidden layers through the residual connection, thus the hidden layers enforces learner to minimize a residual image between the source and target images, which usually is noise and artifacts.[26, 45, 89, 108, 152] In contrast, dense block concatenates outputs from previous layers instead of using the summation, to connect adjacent layers in a feed-forward fashion. It is able to capture multi-frequency (high frequency and low frequency) information to well-represent the mapping from source image modality to target image modality, thus it is commonly used in inter-modality image synthesis such as MR-to-CT, and PET-to-CT.[25, 27, 90, 104, 105, 106]

CNN and its variants are commonly used for the generative and the discriminative networks. Emami *et al.* used ResNet for its generative network.[30] They removed the fully connected layers and added two transposed convolutional layers after residue blocks as deconvolution. Kim *et al.* combined the U-net and the residual training scheme in the generative network.[74] Olberg *et al.* proposed a deep spatial pyramid convolutional framework that includes an atrous spatial pyramid pooling module in a U-net architecture. The module performs atrous convolution at multiple rates in parallel such that multiscale features can be exploited to characterize a single pixel.[125] The encoder is then able to capture rich multiscale contextual information, which aids the image translation. Compared with generator, the discriminator is mostly implemented in a simpler form. A typical example is a few down-sampling convolutional layers followed by a sigmoid layer to binarize the output, as proposed by Liu *et al.*[105]

In addition to the image quality and accuracy loss functions as in U-net, adversarial loss functions are incorporated in GAN and its variants. The adversarial term, unlike the reconstruction term that

represents image intensity accuracy, reflects the correct or wrong decision that the discriminator makes on real image or synthetic image. Apart from the binary cross entropy mentioned above or a similar form of sigmoid cross entropy, the negative log likelihood functions from the original publication of GAN in computer vision are also widely used. However, the training process may suffer from divergence caused by vanishing gradient and mode collapse when discriminator is trained to be optimal for a fixed generator.[168] Emami *et al.* proposed to use least square loss that has been shown to be more stable during training and generates higher quality results.[30] Loss function using Wasserstein distance can be another option since it has smoother gradient flow and better convergence than the original one.[168] It has also been shown that in GAN, simply providing the true or fake labels by the discriminator may not be sufficient for the generator to improve, which causes instability in training due to gradient vanishing and exploding. Ouyang *et al.* employed a feature matching technique by specifying a new objective such that the generator encourages the synthesized images to match the expected value of features on the intermediate layers of discriminator, instead of directly maximizing the final output of the discriminator.[126]

3.4 Other

In addition to the above architectures, other designs have also been proposed to adapt to specific applications in the reviewed studies. For example, Zhang *et al.* proposed a dual-domain CNN framework that uses two parallel CNNs in spatial and frequency domains respectively and interacts with each other by Fourier transform for generating synthetic 7T MRI from 3TMRI.[180] The additional integration of frequency domain was proved to be superior to using spatial domain alone in synthesis accuracy. In the study of reconstructing ultra-low-dose amyloid PET reconstruction by Ouyang *et al.*, a pretrained classifier that predicts the amyloid status (positive or negative) is incorporated into a GAN-based network. The pretrained amyloid status classifier acts as a feature extractor and provides feature maps in the calculation of perceptual loss combined in GAN.

Using images from multiple modalities as input in deep learning network has been shown effective in providing more useful features for learning and testing in several studies. These multi-modality images are usually treated as inputs with multiple channels in the first layer, each of which has a spatial invariant kernel applied for convolution on the entire image. Wang *et al.* claimed that the contributions of different modalities could vary at different locations, thus they added a locality adaptive fusion network that takes two modalities (a low counting PET and a T1-weighted MRI in their study) as input to generate a fused image by learning different convolutional kernels at different image locations. The fused image is then fed into the generative network in GAN architecture.[160] In contrast to common multi-channel inputs in a single path, Tie *et al.* used three MR images with different contrast as multi-channel inputs in a multi-path architecture which has three training paths in the encoder and each channel has its own feature network.[146] The separate image feature extractions on different MR images are able to avoid the loss of unique features that may be merged in the low level.

4 APPLICATION AREAS

The reviewed articles were categorized into two main groups in this study based on their study objectives: inter-modality (56%) and intra-modality (44%). In each group, there are subgroups that specify the imaging modalities and clinical applications.

4.1 Inter-modality

The group of inter-modality includes the studies of image synthesis from one image modality to a different one, such as from MR to CT, from CT to MR, from PET to CT, and etc. We also consider the transformation between CT and CBCT as inter-modality since they are acquired from different machines with different hardware, and are reconstructed with different principles and algorithms. Based on the studies image modalities, studies in this group were further divided into 4 subgroups, including MR-to-CT, CT/CBCT-to-MR, CBCT-to-CT and PET-to-CT. As shown in Figure 3, MR-to-CT synthesis,

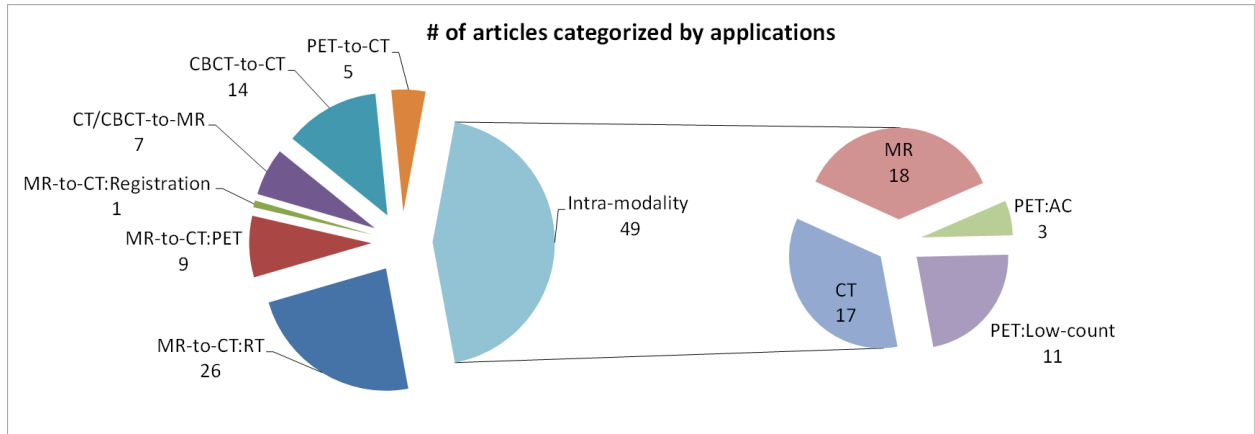


Figure 3. Pie chart of numbers of articles in different categories of applications. MR-to-CT: RT, MR-to-CT: PET and MR-to-CT: Registration represent MR to CT image synthesis used in radiotherapy, PET and image registration, respectively. PET: AC and PET: Low-count represent PET image synthesis used in attenuation correction and low-count to full-count, respectively.

including its applications in radiation therapy, PET and image registration, accounts for about 2/3 of all studies and more than half in inter-modality studies.

4.1.1 MR-to-CT

Image synthesis from MR to CT is one of the first applications that utilize deep learning for medical image synthesis, and remains the most common topic in this field. Motivated by its success, a variety of applications aiming at transformation among other imaging modalities has been actively investigated. The main clinical motivation of MR-based synthetic CT is to replace CT by MR acquisition.[171] The image quality and appearance of the synthetic CT in current studies are still considerably different from real CT, which prevents it from direct diagnostic usage. However, many studies demonstrated its utility for non- or indirect diagnostic purpose, such as treatment planning for radiation therapy and PET attenuation correction.

In current radiation therapy workflow, both MRI and CT are performed on patients for treatment planning. MR images feature excellent soft tissue contrast that is useful for delineation of the tumor and organs at risk (OARs),[71] while CT images provide electron density maps for dose calculation and reference images for pre-treatment positioning. The contours from MR images are propagated to CT images by image registration for treatment planning. However, using both imaging modalities not only leads to additional cost and time for the patient but also introduces systematic positioning errors up to 2 mm during the CT-MRI image fusion process.[124, 149, 150] Moreover, CT scan also introduces non-negligible ionization dose to patients,[21] especially those requiring re-simulation. Thus, it is highly desirable to bypass CT scans with a solely MRI-based treatment planning workflow. Emerging MR-Linac technology also motivates the exclusive use of MRI in radiotherapy.[31, 81] MR cannot replace CT in radiotherapy since the signal of MR images is from hydrogen nucleus, thus cannot provide material attenuation coefficients for electron density calibration and subsequent dose calculation.

Replacing CT with MR is also preferable in current PET imaging although CT is widely combined with PET in order to perform both imaging exams serially on the same table. The CT images are used to derive the 511 keV linear attenuation coefficient map to model photon attenuation by a piecewise linear scaling algorithm [13, 75]. The linear attenuation coefficient map is then used to correct for the loss of annihilation photons by attenuation processes in the object on the PET images to achieve a satisfactory image quality. MR has been proposed to be incorporated with PET as a promising alternative to existing PET/CT system for its advantages of superior soft tissue contrast and radiation dose-free, with a similar challenge as in radiation therapy that MR images cannot be directly used to derive the 511 keV attenuation coefficients for attenuation correction process. Therefore, MR-to-CT image synthesis could be used in PET/MR system for photon attenuation correction.

The missing of a one-to-one relationship between MR voxel intensity and CT HU values leads to a huge difference in image appearance and contrast, which makes intensity-based calibration methods

fail. For example, bone is bright and air is dark on CT, while both are dark on MR. Conventional methods proposed in literatures either segment the MR images into several types of materials and then assign corresponding CT HU numbers,[51, 63, 65, 77, 82, 88] or register the MR images with an atlas with known CT HU numbers.[28, 142, 148] These methods heavily rely on the performance of segmentation and registration, which is always challenging due to the ambiguous air/bone boundary and large inter-patient variation, respectively.

Table I and II listed the studies that synthesized CT images from MR for radiation therapy and PET attenuation correction, respectively. For synthetic CT in radiation therapy, the MAE is the most common and well-defined metrics by which almost every study reported the image quality of its synthetic CT. For synthetic CT in PET AC, the quality of PET with attenuation corrected by synthetic CT is more evaluated than the synthetic CT itself. For studies which presented several variants of methods, we listed the one with best MAE for radiation therapy, and best PET quality for PET AC.

4.1.1.1 Synthetic CT quality

In most of the studies, the MAE of the synthetic CT within patient body in about 40 to 70HU. Some of the reported results are comparable to the typical uncertainties observed in CT simulation. For example, the MAE of soft tissue reported in ref [18, 22, 23, 30, 34, 40, 84] are less than 40 HU. In contrast, the MAE of bone or air is more than 100 HU. The relatively poor performance on bone and air is expected due to their indistinguishable contrast on MR images. Another possible reason can be the misalignment between the CT and MR images in the patient datasets. The misalignment, which mostly happens on the bone, not only cause the intensity mapping error during the training process, but also leads to overestimation of error in the evaluation study since the error from misalignment was counted as synthesis error. Two studies also reported much higher MAE of rectum (70HU) than soft tissue,[4, 84] which may also be attributed to its mismatch on CT and MR due to different filling status. Moreover, considering that the number of bone pixels are much less than those of soft tissue in patient body, the training process tends to map pixels to low HU region in the prediction stage. Potential solutions can be assigning higher loss weights on bone or adding bone-only images for training.[34]

Compared with the conventional methods, learning-based methods demonstrated superior performance in synthetic CT accuracy in multiple studies, which indicates the advantage of the data-driven approaches over model-based methods. [4, 18, 42, 120] For example, the synthetic CT by atlas-based method was shown to be noisier and prone to error of registration, which led to significantly higher MAE than learning-based methods. However, atlas-based methods were shown to be more robust than learning-based methods to image quality variation in some cases.[4] One of the limitations of learning-based method is that its performance can be unpredictable when applied on datasets that are very different from the training datasets. The difference may come from abnormal anatomy, images with degraded quality due to severe artifacts and noise. Atlas-based methods, on the other hand, generate a weighted average of templates from its prior knowledge, thus are less likely to completely fail on unexpected cases.

The reported results among these studies cannot be fairly compared because of different datasets, training and testing strategy, and etc. Thus, it is difficult to conclude the best method of performance. Some studies compared their proposed methods with other competing methods using same datasets, which may reveal the advantages and limitations of those methods. For example, a GAN-based method was shown to preserve better details, be more similar to real CT, and less noisy than a CNN-based method on a cohort of 15 brain cancer patients.[30] Specifically, GAN-based synthetic CT was more accurate at bone/air interfaces and fine structures, with around 10 HU less in MAE. Largent *et al.* compared U-net and GAN with different loss functions on 39 prostate patients: U-net with L2-norm loss, U-net with single-scale perceptual loss, GAN with L2 loss, GAN with single-scale perceptual loss, GAN with multiscale perceptual loss, and GAN with weighted multiscale perceptual loss. Quantitative results showed that the U-net methods had significantly higher MAE than their GAN counterparts. The perceptual loss in U-net and GAN did not help decrease MAE, nor provide any benefits for dose calculation accuracy. Lei *et al.* compared CycleGAN and GAN-based method on brain and prostate cancer patients. Significant improvement of MAE was observed on CycleGAN results, with better visual results on fine structural details and contrast. CycleGAN results, which were less sensitive to local mismatch in the training CT/MR pairs, have less blurry bone boundaries than GAN results. Similar comparison results can also be found in the study of Liu *et al.* where CycleGAN and GAN were compared on liver

SBRT cases.[104] However, the dosimetry study showed minimal difference, which can be contributed to the VMAT plans that are not sensitive to HU inaccuracy.

Among the reviewed studies, different types of MR sequences have been adopted for synthetic CT generation. The specific MR sequence used in each study usually depends on the accessibility. The optimal sequence yielding the best performance has not been studied. T1-weighted and T2-weighted sequences are two of the most common MR sequences used in diagnosis. Due to their wide availability, learning model can be trained from a relatively large number of datasets with CT and co-registered T1- or T2-weighted MR images. T2-w images may be preferable than T1-w since they intrinsically have better geometric accuracy in regions where subject-induced susceptibility is large, such as nasal cavity, and have less chemical shift artifacts at fat and tissue boundaries. However, air and bone have little contrast in either T1- or T2-weighted MR images, which may impede the extraction of the corresponding features in learning-based methods. Two-point Dixon sequence can separate water and fat, which is suitable for segmentation. It has already been applied in commercial PET/MR scanner with combination of volume-interpolated breath-hold examination (VIBE) for Dixon-based soft-tissue and air segmentation for PET AC as a clinical standard.[33, 55] Its drawback is again the poor contrast of bone, which results in the misclassification of bone as fat. In order to enhance the bone contrast to facilitate the feature extraction in learning-based methods, ultrashort echo time (UTE) and/or zero echo time (ZTE) MR sequences have been recently used due to its capability to generate positive image contrast from bone.[100] Ladefoged *et al.* and Blanc-Durand *et al.* demonstrated the feasibility of UTE and ZTE MR sequences using U-net in PET/MR AC, respectively.[8, 80] However, neither of the two studies compared the using of UTE/ZTE and conventional MR sequence under the same deep learning network. Thus, the advantage of this specialized sequence has not been validated. Moreover, compared with conventional T1-/T2-weighted MR images, the UTE/ZTE MR images have little diagnostic value on soft tissue while have a long acquisition time, which may hinder its utility in time-sensitive cases such as whole-body PET/MR scans.

Other studies attempted to use multiple MR images with different contrast as input in training and prediction since it is believed to be superior to single MR sequence in synthetic CT accuracy by providing additional features to the network. Qi *et al.* proposed to use a 4-channel input that includes T1w, T2w, contrast-enhanced T1w, and contrast-enhanced T1w Dixon water images. Compared with the results from fewer channels, 4-channel result has lower MAE.[129] Florkow *et al.* investigated single and multi-channel input using magnitude MR images and Dixon reconstructed water, fat, in-phase and opposed-phase images obtained from a single T1w multi-echo gradient-echo acquisition.[32] They found multi-channel input is able to improve synthetic CT generation than single-channel input. Among the multi-channel input configurations that they tested, the Dixon input outperformed the others. Tie *et al.* used T2-w and pre- and post-contrast T1w MR images in a multi-channel multi-path architecture, and showed a significant improvement over multi-channel single-path and single-channel results.[146] An attractive combination is UTE/ZTE and Dixon, which provide contrast of bone against air and fat against soft tissue, respectively. [39, 95] Leynes *et al.* showed that the synthetic CT using ZTE and Dixon MR has less error than that using Dixon alone.[95] Although the image quality improvement has been validated, the necessity of performing additional MR sequences for synthetic CT generation needs to be further evaluated in specific applications since it usually requires extra cost and acquisition time.

In the reviewed studies, the CT and MR images in the training datasets were acquired separately on different machines. Thus, image registration is required between the CT and MR to create CT-MR pairs for training. The registration error is minimal at brain, and starts becoming an issue at pelvis due to different filling status in bladder and rectum, then be challenging in abdomen due to the variation introduced by respiratory and peristalsis. U-net and GAN-based methods are susceptible to registration error if using a pixel-to-pixel loss. Kazemifar *et al.* proposed a possible solution that uses mutual information as the loss function in the generator of GAN to bypass the registration step in the training.[70] As CycleGAN was originally developed for unpaired image-to-image translation, CycleGAN-based methods feature higher robustness to registration error since it introduces cycle consistency loss to enforce the structural consistency between original one and cycle one, (e.g., force cycle MRI generated from synthetic CT to be the same as original MRI).[27, 48, 89, 93]

4.1.1.2 MR-only radiation therapy

For the studies aiming for radiation therapy, many of them evaluated the dosimetry accuracy of synthetic CT by calculating radiation treatment dose using same treatment plan and comparing it with that on real CT as ground truth. It is shown that the dose difference is about 1%, which is small when compared with the current total uncertainty of dose delivery on patient (5%) during the entire radiation therapy pathway. Compared to the large improvement of image accuracy, the improvement from learning-based methods over conventional methods in dosimetry accuracy on photon radiation therapy is relatively small. The conclusion about the significance of the improvement is also mixed.[4, 18] A potential reason is that the dose calculation on photon plans is quite forgiving to image inaccuracy, especially at homogeneous regions such as brain. For the widely studied volumetric modulated arc therapy (VMAT), the contribution from errors in images to dose also tends to cancel out in an arc. However, the small dosimetric improvement may still be worthwhile in cases such as SRS and SBRT where a large amount of dose is to be delivered into a small volume. In such cases, the dose calculation accuracy could be sensitive to the errors on synthetic CT around the target volume.[156] The recent adoption of non-coplanar beams may also be challenging to MR-based synthetic CT since the beam path length can be sensitive to the prediction error of patient surface due to the beam obliquity, which is worth further investigation.

Studies have also evaluated the synthetic CT in the context of proton radiation treatment for prostate, liver and brain cancer.[105, 106, 136] Unlike photon, proton beams deposit dose with a very high dose gradient at the distal end of the beam. The proton treatment plan thus has highly conformal dose distribution to the target by proton beams coming from several angles. The local HU inaccuracy along the beam path on the planning CT would lead to shift of the highly conformal high-dose area, which may cause tumor to be substantially under-dosed or the organs-at-risk to be over-dosed.[96] As shown in the Figure 4 in ref [106], most dose difference of using synthetic CT was at the distal end of the proton beam. As reported by Liu *et al.*,[105, 106] the largest and mean absolute range difference is 0.56 cm and 0.19 cm among their 21 liver cancer patients, and 0.75 cm and 0.23 cm among 17 prostate cancer patients.

In addition to dosimetry accuracy for treatment planning, another important aspect for the evaluation of synthetic CT is its geometry fidelity for patient setup. Unfortunately, the studies on synthetic CT positioning accuracy are sparse. Fu *et al.* conducted patient alignment test by rigidly aligning the synthetic CT and real CT to the CBCT acquired at the first fraction.[34] The translation vector distance and absolute Euler angle difference between the two alignments were found to be less than 0.6mm and 0.5° on average, respectively. Gupta *et al.* adopted a similar study, and found the translation difference was less than 0.7mm in one direction.[40] Apart from alignment with CBCT, the alignment between the derived DRR from synthetic CT and kV image of patient is also of clinical interest. However, no study on DRR alignment accuracy is found in the reviewed literatures. Note that the geometry accuracy of synthetic CT is not only affected by the performance of methods, but also the geometric distortion on MR images caused by magnetic field inhomogeneity as well as subject-induced susceptibility and chemical shift. Methods to mitigate the MR distortion are also important in improving synthetic CT accuracy in patient positioning.

4.1.1.3 PET attenuation correction

For the studies aiming for PET attenuation correction, the bias on PET quantification caused by the synthetic CT error has been evaluated. Although it is difficult to specify the tolerance level of quantification error before it affect clinicians judgment, the general consensus is that quantification errors of 10% or less typically do not affect diagnosis.[49] Based on the average relative bias represented by these studies, almost all of the proposed methods in the studies met this criterion. However, it should be noted that due to the variation among study objects, the bias in some volume-of-interests (VOIs) of some patients may exceed 10%.[8, 95] It suggests that special attention should be given to the standard deviation of bias as well as its mean when interpreting results since the proposed methods may have poor local performance that would affect some patients. On the other hand, listing or plotting the results of every data points, or at least the range, instead of simply giving a mean±STD in presenting results, would be more informative in demonstrating the performance of the proposed methods.

Since bone has the highest attenuation capability due to its high density and atomic number,[170] its accuracy on synthetic CT plays a vital role in the final accuracy of the attenuation corrected PET. Compared with the evaluation for radiation therapy, the bias and geometry accuracy of bone on the

synthetic CT is more often evaluated for PET AC. Multiple studies showed that synthetic CT with better bone accuracy tends to generate more accurate PET globally.[5, 8, 39, 147] The more accurate synthetic CT images by learning-based methods than conventional methods also lead to a more accurate PET AC. Such improvements were found to be significant in the reviewed studies. It was shown that PET AC by conventional synthetic CT methods have about 5% bias on average among selected VOIs, while for learning-based methods, the bias was reduced to around 2%.[39, 56, 95, 100, 147]

In addition to the two widely studied applications, i.e. radiation treatment simulation and PET AC, using synthetic CT from MR to aid intra-modality image registration has been proved promising. Direct image registration between CT and MR is very challenging due to the distinct image contrast, and can be unreliable in deformable registration algorithms where large distortion is allowed. McKenzie *et al.* proposed a CycleGAN-based network to generate synthetic CT, and used the synthetic CT to replace the MR in MR-CT registration for head-and-neck.[116] In this way, the multimodality registration problem is reduced to a mono-modality one. In their study as summarized in Table III, it was found that with the same deformable registration algorithm, the average landmark error decreased from 9.8 ± 3.1 mm in direct MR-CT registration to 6.0 ± 2.1 mm in using synthetic CT as bridge. Similar results were also found in the registration at CT-MR direction.

Table I. Summary of studies on MR-based synthetic CT for radiation therapy

Network	MR parameters	Site, and # of patients in training/testing	Key findings in image quality	Key findings in dosimetry	Author, year
U-net	1.5T T1w without contrast	Brain: 18, 6-fold cross validation	MAE (HU): 84.8 ± 17.3	N/A*	Han, 2017 [42]
GAN	N/A	Brain: 16 Pelvis: 22	MAE (HU): 92.5 ± 13.9	N/A	Nie <i>et al.</i> , 2018[120]
CNN	T1w	Brain: 16, leave-one-out Pelvis: 22, leave-one-out	MAE (HU): 85.4 ± 9.24 (brain) 42.4 ± 5.1 (Pelvis)	N/A	Xiang <i>et al.</i> , 2018[165]
CNN	1.5T T1w	Brain: 52, 2-fold cross validation	MAE (HU): 67 ± 11	Dose difference <1%	Dinkla <i>et al.</i> , 2018[23]
U-net	3T T2w	Pelvis: 39, 4-fold cross validation	MAE (HU): 32.7 ± 7.9	Dose difference <1%	Arabi <i>et al.</i> , 2018 [4]
U-net	3T T2w	Pelvis: 36 training/15 testing	MAE (HU): 29.96 ± 4.87	Dose difference of max dose in PTV <1.01%	Chen <i>et al.</i> , 2018 [18]
GAN	1T post-Gadolinium T1w	Brain: 15, 5-fold cross validation	MAE (HU): 89.3 ± 10.3	N/A	Emami <i>et al.</i> , 2018[30]
GAN	Dixon in-phase, fat and water	Pelvis: 91 (59 prostate+18 rectal+14 cervical cancer), 32 (prostate) training/59 (rest) testing	MAE (HU): 65 ± 10 (Prostate) 56 ± 5 (Rectum) 59 ± 6 (Cervix)	Dose difference < 1.6%	Maspero <i>et al.</i> , 2018 [114]

U-net	3T in-phase Dixon T2w	Head and neck: 22 training/12 testing	MAE (HU): 75±9	Mean dose difference - 0.03%±0.05% overall, -0.07%±0.22% in >90% of prescription dose volume	Dinkla <i>et al.</i> , 2019[22]
U-net	1.5T T1w without contrast	Pelvis: 20, 5-fold cross validation	MAE (HU): 40.5±5.4 (2D) 37.6±5.1 (3D)	N/A	Fu <i>et al.</i> , 2019[34]
U-net	3T in-phase Dixon T1w	Brain: 47 training/13 testing	MAE (HU): 17.6±3.4	Mean target dose difference 2.3±0.1%	Gupta <i>et al.</i> , 2019[40]
GAN	1.5T post-Gadolinium T1w	Brain: 77, 70% training/12% validation/18% testing	MAE (HU): 47.2±11.0	Mean DVH metrics difference <1%	Kazemifar <i>et al.</i> , 2019[70]
GAN	3T T2w	Pelvis: 39, training/testing: 25/14, 25/14, 25/11	MAE (HU): 34.1±7.5	PTV V95% difference < 0.6%	Largent <i>et al.</i> , 2019[84]
CycleGAN	Brain: T1w Pelvis: T2w	Brain: 24 Pelvis: 20 Leave-one-out cross validation	MAE (HU): 55.7±9.4 (Brain) 50.8±15.5 (Pelvis)	N/A	Lei <i>et al.</i> , 2019[90]
U-net	1.5T T1w	Brain: 30 training/10 testing	MAE (HU): 75±23	PTV V95% difference 0.27%±0.79%	Liu <i>et al.</i> , 2019[103]
CycleGAN	3T/1.5T T1w	Liver: 21, leave-one-out cross validation	MAE (HU): 72.87±18.16	Mean DVH metrics difference <1% for both photon and proton plans	Liu <i>et al.</i> , 2019[104] and Liu <i>et al.</i> , 2019[106]
CycleGAN	1.5T T2w	Pelvis: 17, leave-one-out cross validation	MAE (HU): 51.32±16.91	Mean DVH metrics difference <1% (Proton plan)	Liu <i>et al.</i> , 2019[106]
U-net	1.5T T1w	Brain: 57 training/28 validation/4 testing	MAE (HU): (82, 147) ⁺	Gamma passing rate: >95% at (1%, 1mm) for photon plan, >90% at (2%, 2mm) for proton plan	Neppl <i>et al.</i> , 2019[118]
GAN	0.35T T1w	Breast: 48 training/12 testing	MAE (HU): 16.1±3.5	PTV D95 difference <1%	Olberg <i>et al.</i> , 2019[125]
CycleGAN	1.5T T1w	Brain: 50	MAE (HU): 54.55±6.81	PTV D95 difference <0.5% (proton plan)	Shafai-Erfani <i>et al.</i> , 2019[136]
U-net	1.5T T2w	Head and neck: 23 training/10 testing	MAE (HU): 131±24	N/A	Wang <i>et al.</i> , 2019[158]

U-net	3T T1w Dixon	Pelvis: 27, 3-fold cross validation	MAE (HU): (33, 40)	N/A	Florkow <i>et al.</i> , 2020[32]
GAN	T1w+T2w+ FLAIR	Brain: 15	MAE (HU): 108.1±24.0	DVH metrics difference < 1%	Koike <i>et al.</i> , 2020[76]
GAN	T1w+T2w+ Contrast- enhanced T1w+ Contrast- enhanced T1w Dixon water	Head and neck: 30 training/15 testing	MAE (HU): 69.98±12.02	Mean average dose difference <1%	Qi <i>et al.</i> , 2020[129]
GAN	1.5T Pre contrast T1w+post contrast T1w+T2w	Head and neck: 32, 8-fold cross validation	MAE (HU): 75.7±14.6	N/A	Tie <i>et al.</i> , 2020[146]
GAN	1.5T and 3T T2w from three scanners	Pelvis: 11 train- ing from two scanner/8 testing from one scanner	MAE (HU): 48.5±6	Maximum dose difference in tar- get = 1.3%	Boni <i>et al.</i> , 2020 [12]

*N/A: not available, i.e. not explicitly indicated in the publication

+Numbers in parentheses indicate minimum and maximum values.

Table II. Summary of studies on MR-based synthetic CT for PET attenuation correction.

Network	MR param- eters	Site, and # of patients in train- ing/testing	Key findings in synthetic CT quality	Key find- ings in PET quality	Author, year
U-net	Dixon and ZTE	Brain: 14, leave-two-out	MAE (%): 12.62±1.46	Absolute bias <3% among 8 VOIs	Gong <i>et al.</i> , 2018[39]
U-net (Encoder- decoder)	3T UTE	Brain: 30 pre-training/6 training/8 testing	N/A*	Bias (%): -0.8±0.8 to 1.1±1.3 among 23 VOIs	Jiang <i>et al.</i> , 2018[56]
U-net	3T Dixon and ZTE	Pelvis:26, 10 training/16 testing	Mean error (HU): -12±78	RMSE (%): 2.68 among 30 bone lesions, 4.07 among 60 soft-tissue lesions	Leynes <i>et al.</i> , 2018[95]
U-net (Encoder- decoder)	1.5T T1w	Brain: 30 training/10 testing	N/A	Bias (%): -3.2±1.3 to 0.4±0.8	Liu <i>et al.</i> , 2018[100]
U-net	1.5T T1w	Brain: 44 training/11 validation/11 testing	Global Bias (%): -1.06±0.81	Global Bias(%): -0.49±1.7 for 11C-WAY- 100635 -1.52±0.73 for 11C- DASB	Spuhler <i>et al.</i> , 2019[144]

U-net	Dixon-VIBE	Pelvis: 28 pairs from 19 patients, 4-fold cross validation	MAE (%): 2.36±3.15	Bias (%): 0.27±2.59 for fat -0.03±2.98 for soft tissue -0.95±5.09 for bone	Torrado-Carvajal <i>et al.</i> , 2019[147]
U-net	ZTE	Brain: 23 training/47 testing	N/A	Bias (%): -1.8±1.9 to 1.7±2.6 among 70 VOIs	Blanc-Durand <i>et al.</i> , 2019[8]
U-net	UTE	Brain: 79 (pediatric), 4-fold cross validation	N/A	Bias (%): -0.2 to 0.5 in 95% CI	Ladefoged <i>et al.</i> , 2019[80]
GAN	3T T1w	Brain: 40, 2-fold cross validation	MAE (HU): 302±79 (bone)	Absolute bias < 4% among 63 VOIs	Arabi <i>et al.</i> , 2019[5]

*N/A: not available, i.e. not explicitly indicated in the publication

Table III. Summary of studies on MR-based synthetic CT for registration.

Network	MR parameters	Site, and # of patients in training/testing	Key findings in synthetic CT quality	Key findings in registration accuracy	Author, year
CycleGAN	0.35T	Head and neck: 25, 5-fold cross validation	N/A*	landmark error (mm): 6.0±2.1 (MR-to-CT) 6.6±2.0 (CT-to-MR)	McKenzie <i>et al.</i> , 2019[116]

*N/A: not available, i.e. not explicitly indicated in the publication

4.1.2 CT/CBCT-to-MRI

Due to the superior soft tissue contrast on MRI, it is attractive to generate synthetic MRI from CT or CBCT in applications that are sensitive to soft tissue contrast, such as segmentation.[173] Comparing with synthesizing CT from MR, synthesizing MR from CT/CBCT seems more challenging since MR contains much more contrast and details that need to be recovered but are not shown on CT images. Deep learning methods, however, are quite competent in mapping high non-linearity, which makes the proposed application possible.

As listed in Table IV, the related studies in the reviewed literatures adopted similar networks as MR-to-CT synthesis. In most studies, the generated synthetic MR served as a bridge that is used in other applications, thus the image intensity accuracy of synthetic MR was not reported. In studies that reported synthetic MR accuracy, MAE is less meaningful than other image similarity metrics such as PSNR since the MR image intensity is relative.

Jiang *et al.* proposed to use synthetic MR to augment the training data for MR tumor segmentation in lung.[58] In their study, 81 MR image sets have tumor contours delineated by experts, which was considered as a small data size for training a segmentation model. In order to enlarge the training datasets, they employed a GAN-based model to generate synthetic MR from 377 CT image sets which

has tumor labelled using other groups of unpaired MR image sets. The 377 synthetic MR image sets with tumor labels were then incorporated into segmentation model training. The addition of synthetic MR in training dataset was shown to be beneficial in improving the tumor segmentation performance. It increased the DSC of tumor to 0.75 ± 0.12 from 0.50 ± 0.26 in which synthetic MR was not included in training datasets. The study also showed that among the synthetic MRIs generated by different methods, the ones closer to real MR enabled better segmentation results.

In the training stage of segmentation model in the above study, the training target contours for the synthetic MRIs were not delineated based on MR but on CT. Thus, in the testing stage, the output contours were also expected to be CT-based rather than MR-based. Since the delineation of tumor relies on the image contrast, the contour for a same object is usually different on CT and MRI. In some cases, contours from MR is more accepted as golden standard due to its superior soft tissue contrast than those on CT. Using CT-based contours as training target for synthetic MR may not only confuse the network, but also waste the superior soft tissue contrast of MRIs.

In the studies of Dong *et al.* and Lei *et al.*, the synthetic MRIs were used as a bridge to facilitate segmentation on CT/CBCT images.[25, 91, 94] The segmentation targets in their study include prostate, which has low contrast on CT/CBCT but high on MRI images, and tends to be over-contoured with larger variation on CT/CBCT images when compared with using MRI only or CT+MRI.[128, 151] The synthetic MRIs generated by CT were then aimed at providing superior soft tissue contrast for prostate segmentation. In their studies, paired CT and MRI image sets were used, and the prostate contours used as training targets and ground truth for synthetic MR were delineated on MR or both CT and MRI. It shows that the mean DSC of prostate between segmentation results and ground truth increased from 0.82 ± 0.09 of direct segmentation on CT to 0.87 ± 0.04 of segmentation on synthetic MR with statistical significance.

Table IV. Summary of studies on CT/CBCT-based synthetic MR.

Network	MR parameters	Site, and # of patients in training/testing	Key findings in synthetic MR quality	Application	Author, year
CycleGAN	T2w	Pelvis: 140, 5-fold cross validation	N/A*	Male pelvis multi-organ segmentation on CT	Dong <i>et al.</i> , 2019[25]
GAN	3T T2w	Lung: 42 MRIs and 377 CTs, unpaired training	Kullback–Leibler divergence in tumor: 0.069	Augment training data for lung tumor segmentation on MR	Jiang <i>et al.</i> , 2019[58]
CycleGAN	3T T2w	Spine: 549 training/92 testing	PSNR(dB): 64.553 ± 1.890	Diagnosis	Jin <i>et al.</i> , 2019[59]
CycleGAN	3T T2w	Brain: 192 training/10 testing	PSNR(dB): 65.35	Diagnosis	Jin <i>et al.</i> , 2019[60]
GAN	1.5T and 3T T2w	Spine: 280 pairs in training/15 testing	PSNR(dB): 64.9 ± 1.86	Diagnosis	Lee <i>et al.</i> , 2020[87]
CycleGAN	1.5T T2w	Pelvis: 49, leave-one-out	N/A	Prostate segmentation on CT	Lei <i>et al.</i> , 2020[94]

CycleGAN	T2w	Pelvis: 100, 5-fold cross validation	N/A	Male pelvis multi-organ segmentation on CBCT	Lei <i>et al.</i> , 2020[91]
----------	-----	--------------------------------------	-----	--	------------------------------

*N/A: not available, i.e. not explicitly indicated in the publication

4.1.3 CBCT-to-CT

CBCT and CT share a common basic physics principle of X-ray attenuation and image reconstruction concept of back projection. However, they are different in the detailed implementation of acquisition and reconstruction, and clinical utility, thus they are considered as two image modalities in this review study.

CBCT has been increasingly utilized in image-guided radiation therapy to improve treatment performance. CBCTs are acquired at the time of treatment delivery and provide detailed anatomic information in the treatment position. In clinical practice, CBCT is primarily used to determine the degree of patient setup error and inter-fraction motion by comparing the displacement of anatomic landmarks from the treatment planning CT images.[7] More demanding applications of CBCT have been proposed with the increasing use of adaptive radiation therapy, such as daily estimation of delivered dose based on CBCT images, and automatic contouring on CBCTs based on a deformable image registration (DIR) with the pCT.[2, 184]

Unlike CT scanners using fan-shaped X-ray beam with multi-slice detectors, CBCT uses cone-shaped X-ray beam with a flat panel detector. The flat panel detector features a high spatial resolution and a wide coverage along the z-axis, but also gets more scatter signals since the scatter X-ray generated from the entire volume can reach the detector. The scatter signals cause severe streaking and cupping artifacts on the CBCT images and lead to significant CT number errors. Such errors complicate the calibration process of CBCT Hounsfield Unit (HU) to electron density for dose calculation.[112] The degraded image contrast and the suppression of bone CT number can also cause large errors in DIR for contour propagation from planning CT to CBCT.[50] The significantly degraded image quality of CBCT prevents it from those advanced quantitative usage in radiation therapy.

Many correction methods for CBCT shading artifacts have been proposed, including hardware-based pre-processing methods[111, 140, 141] and software-based post-processing techniques [9, 19, 79, 121, 172, 183] These methods enhance the scatter correction performance, while their implementations entail combined considerations of computational complexity, imaging dose, scan time, practicality, and efficacy. With these correction methods, residual artifacts are still commonly observed in clinical CBCT images. Moreover, most of the existing methods cannot restore the true Hounsfield Unit (HU) value in CBCT images; i.e., the pixel values in CBCT images are not calibrated identically to planning CT images in the treatment planning system for dose calculation.

Deep learning-based methods, as listed in Table V, have been proposed to correct and restore the CBCT HU values to be close to those of CT by exploiting its outstanding image translation abilities. CBCT images are reconstructed from hundreds of 2D projections from different angles. A few studies applied the neural network in the projection domain in order to enhance the quality of the projection images prior to volume reconstruction. More studies directly converted the reconstructed CBCT image volumes into high quality as CT. Projection-domain methods can be advantageous in a larger number of training projections (>300) than training images of image domain (<100) for each scan. Moreover, the appearances of cupping and streaking artifacts caused by scatter on CBCT images are more random and diverse among different patients than the distribution of scatter photons on projection images. In other words, the scatter presented on projection is more predictable and easier to learn for neural networks. The image-domain methods do not train models on non-anthropomorphic phantom since it is useless for patient image sets due to the huge difference in image features. However, such difference in image features is much less in projection domain. Nomura *et al.* showed that the features characterizing scatter distribution in anthropomorphic phantom projections can be learned from non-anthropomorphic phantom projections.[123] The potential reason is that the neural network successfully learned the inherent relationship between the scatter distribution and objective thickness on projection domain. The

relationship between the scatter artifacts and the objective appearance is much more complicated and thus can be hardly learned on image domain.

In the reviewed studies, the learning target of CBCT images/projections is mostly the corresponding CT images/projections that captured on the same patient. However, mismatch is commonly seen between CT and CBCT, thus registration is required to reduce artifact caused by mismatch. Liu *et al.* compared the performance of their method between using rigidly and deformably registered CBCT-CT training data in their pancreas study.[108] They found that synthetic CT by rigidly registered training data had slightly higher in MAE than deformably registered training data (58.45 ± 13.88 HU vs 56.89 ± 13.84 HU, $p > 0.05$), and less noise with better organ boundaries. Kurz *et al.* showed that using unmatched CT and CBCT as training datasets in CycleGAN without pixel-by-pixel loss function is feasible to generate synthetic CT with satisfactory quality.[78] To bypass the registration step, Hansen *et al.* and Landry *et al.* proposed to correct CBCTs by conventional method first, and then use the corrected CBCTs as the learning target. Since the corrected CBCTs are always in the same geometry as original CBCT, registration is no longer needed.[44, 83] However, the quality of the synthetic CT is limited by the conventional method-generated CBCT.

In studies that compared the performance of the proposed deep learning-based methods with conventional CBCT correction methods using same datasets, learning-based methods feature better image quality.[3, 45, 72, 123, 166] Adrian *et al.* found their U-net-based method outperformed two conventional methods, deformable registration method and analytical image-based correction method, with the lowest MAE of synthetic CT, the lowest spatial non-uniformity, and the most accurate bone geometry.[3] Harms *et al.* observed a lower noise of their synthetic CT and a more similar appearance as real CT when compared with a conventional image-based correction method.[45] Conventional correction methods are designed to enhance a specific aspect of image quality, while the learning-based methods, aiming to generate synthetic CT from CBCT, would change every aspect of image quality to be close to CT, such as noise level that is usually not considered in conventional correction methods. A few studies also compared different networks with same patient datasets, and it is shown that CycleGAN outperforms GAN and U-net. [98, 108]

Synthetic CTs are found to have significant improvement over original CBCTs in dosimetry accuracy, and are close to planning CT for photon dose calculation. The feasibility in VMAT photon plans have been evaluated in various sites by investigating selected DVH metrics and dose difference/Gamma difference. Fig. 4 in the study of Liu *et al.* demonstrates that large local dose calculation error happened at locations with severe artifacts, and synthetic CT successfully mitigated the artifacts and therefore the dosimetry error.[108] Compared with photon, the dosimetry accuracy for proton plan is more challenging. Proton range shift on synthetic CT is usually about 3mm and can be up to 5mm. [44, 78, 83]

Table V. Summary of studies on CBCT-based synthetic CT for radiation therapy.

Network	Projection or image domain	Site, and # of patients in training/testing	Key findings in synthetic CBCT quality	Key findings in dosimetry	Author, year
U-net	Projection	Pelvis: 15 training/7 testing/8 evaluation	MAE (HU): 46	Passing rate for 2% dose difference: 100% for photon plan, 15%-81% for proton plan	Hansen <i>et al.</i> , 2018[44]
U-net	Image	Pelvis: 20, 5-fold cross validation	PSNR (dB): 50.9	N/A*	Kida <i>et al.</i> , 2018[72]
CNN	Image	Lung: 15 training/5 testing	PSNR (dB):8.823	N/A	Xie <i>et al.</i> , 2018[166]

U-net	Image	Head and neck: 30 training/7 validation/7 testing Pelvis: 6 training/5 testing	MAE (HU): 18.98 (head and neck) 42.40 (pelvis)	N/A	Chen <i>et al.</i> , 2019[17]
CycleGAN	Image	Brain: 24, leave-one-out Pelvis: 20, leave-one-out	MAE (HU): 13.0±2.2 (brain) 16.1±4.5 (Pelvis)	N/A	Harms <i>et al.</i> , 2019[45]
CycleGAN	Image	Pelvis: 18 training/7 validation/8 testing	MAE (HU): 87 (79, 106) ⁺	Passing rate for 2% dose difference: 100% for photon plan, 71%-86% for proton plan	Kurz <i>et al.</i> , 2019[78]
U-net	Image	Pelvis: 27 training/7 validation/8 testing	MAE (HU): 58 (49, 69)	Passing rate for 2% dose difference: >99.5% for photon plan, >80% for proton plan	Landry <i>et al.</i> , 2019[83]
U-net	Image	Head and neck: 50 training/10 validation/10 testing	MAE (HU): (6, 27)	Average DVH metrics difference: 0.2±0.6%	Li <i>et al.</i> , 2019[97]
CycleGAN	Image	Head and neck: 81 training/9 validation/20 testing	MAE (HU): 29.85±4.94	Gamma passing rate at (1%, 1mm): 96.26±3.59%	Liang <i>et al.</i> , 2019[98]
U-net	Projection	1800 projections in training (simulation)/200 validation (simulation)/360 testing (phantom)	MAE (HU): 17.9±5.7	N/A	Nomura <i>et al.</i> , 2019[123]
U-net	Image	Head and neck: 33, 3-fold cross validation	MAE (HU): 36.3±6.2	Gamma passing rate at (2%, 2mm): 93.75-99.75% (proton)	Adrian <i>et al.</i> , 2020[3]
U-net	Image	Head and neck: 40 training/15 testing	MAE (HU): 49.28	N/A	Yuan <i>et al.</i> , 2020[179]

CycleGAN	Image	Pelvis: 16 training/4 testing	Mean error (HU): (2, 14)	N/A	Kida <i>et al.</i> , 2020[73]
CycleGAN	Image	Pancreas: 30. Leave-one-out	MAE (HU): 56.89±13.84	DVH metrics difference < 1Gy	Liu <i>et al.</i> , 2020[108]

*N/A: not available, i.e. not explicitly indicated in the publication

+Numbers in parentheses indicate minimum and maximum values.

4.1.4 PET-to-CT

In a PET-only scanner where neither CT nor MR is available, transmission scan with an external positron source rotated around the patient is currently used to determine the attenuation of patient body for attenuation correction. It is thus desirable to use the non-attenuation-corrected (NAC) PET to generate synthetic CT to provide anatomical information by the powerful image style transfer ability of deep learning methods. Moreover, for PET/MR, although MR provides anatomical images, the current atlas or registration-based methods in MR-based PET/MR attenuation correction are subject to errors in the bone on the derived attenuation map. Deriving attenuation map from existing NAC PET is therefore an attractive alternative.

The related studies are listed in Table VI. Similar to other synthetic image generation, the synthetic CT images were generated from the NAC PET images using the deep learning model trained by pairs of NAC PET and CT images that were acquired from a PET/CT scanner. Synthesizing CT from NAC PET images is intrinsically challenging since the NAC PET images have much lower spatial resolution than CT and provide little anatomical information. In the studies of Hwang *et al.*, time-of-flight information was used to generate maximum-likelihood reconstruction of activity and attenuation maps as input since they provides more anatomical information than NAC PET.[53, 54] Despite of these difficulties, the reported average errors are all within the 10% consensus tolerance, which is competitive to the results by MR-based synthetic CT.

Whole-body PET scan has been an important imaging modality in finding tumor metastasis. Most of the reviewed studies about image synthesis in PET developed their proposed methods for brain applications. Although the learning-based methods are data-driven and not site-specific, they may not be readily applicable to the whole body due to the high anatomical heterogeneities, large variance of activity among different organs, and inter-subject variability. Hwang *et al.* and Dong *et al.* investigated learning-based whole-body PET AC using synthetic CT generation strategy.[27, 54] Both studies reported average bias on lesion to be around 1%, which is promising for clinical use. Dong *et al.* reported average bias within 5% in all selected organs except >10% in lungs in both studies. The authors attributed the poor performance on lung to the tissue inhomogeneity and insufficient representative training datasets. They also found that the synthetic CTs showed blurriness in lung like respiratory motion artifacts that were not shown on CT, which indicates that synthetic CTs are more matched with PETs than CT and can be more suitable for AC. Both studies are performed for PET-only scanner, and so far, there is no learning-based methods developed for PET/MR whole body scanner. Compared with PET-only scheme, the PET/MR provides the anatomical structural information from MR, while the integration of the additional MR into PET AC can be more challenging than brain scans since the MR may have a limited field of view (FOV), longer scan time that introduces more motion, and degraded image quality due to larger inhomogeneous-field region.

Table VI. Summary of studies on PET-based synthetic CT for PET attenuation correction.

Network	Site, and # of patients in training/testing	Key findings in synthetic CT quality	Key findings in PET quality	Author, year
U-net	Brain: 40, 5-fold cross validation	N/A*	Average 5% error in activity quantification	Hwang <i>et al.</i> , 2018[53]
U-net	Brain: 100 training/28 testing	MAE (HU): 111±16	Bias: <2% among 28 VOIs	Liu <i>et al.</i> , 2018[101]

GAN	Brain: 50 training/40 testing	N/A	Bias: <2.5% among 7 VOIs	Armanious <i>et al.</i> , 2018[6]
U-net	Whole body: 60 training/20 validation/20 testing	Relative error (%): 0.91±3.55 (soft tissue) 0.43±6.80 (bone)	Bias (%): 1.31±3.55 in lesions	Hwang <i>et al.</i> , 2019[54]
CycleGAN	Whole body: 80 training/39 testing	MAE (HU): 108.9±19.1	Bias (%): 1.07±9.01 in lesions	Dong <i>et al.</i> , 2019[27]

*N/A: not available, i.e. not explicitly indicated in the publication

4.2 Intra-modality

The group of intra-modality includes studies that transform between two different protocols within a same imaging modality, such as among different sequences of MRIs, or the restoration of images from low quality protocol to high quality protocol. Studies solely aiming at image quality improvement such as image denoising and artifact correction is not included in this study. Based on the studied image modalities, studies in this group can be further divided into CT, MR and PET groups. As shown in Figure 3, the number of studies on the three imaging modalities is close.

4.2.1 CT

CT imaging dose becomes an increasing public concern nowadays since excessive radiation dose can lead to increased risks of radiation-induced cancer and genetic defects.[11, 99, 119] It is common for patients to undergo multiple CT scans in different procedures of diagnosis and treatment. Thus the accumulated imaging dose can be a big concern, particularly for pediatric patients who are more sensitive to radiation and have longer life expectancy than adults.[10]

CT dose can be lowered by either reducing X-ray exposure (mAs).[109, 145, 153, 154] or the number of X-ray projections.[109, 145, 153, 154] However, if still reconstructing image by conventional filter-backprojection (FBP) algorithm, image quality would be degraded with elevated image noise level and reduced image signal-to-noise ratio for low mAs scheme, or with severe undersampling artifacts for low projection scheme. These low-quality images effects would make routine tasks on CT images difficult for clinicians. Hardware-based methods such as optimization on data acquisition protocol (automatic exposure control) [66] and improvements in detector designs[178] have been shown to be effective in reducing imaging dose to some extent while maintaining clinically acceptable image quality. However, further dose reduction from these techniques is limited by detector physical properties and hence very costly.

Iterative CT image reconstruction algorithms have been proposed for decades to address the degraded image quality resulted from insufficient data acquisition.[127] It models the physical process of a CT scan with prior knowledge, thus is more resilient to noise and require less imaging dose for the same image quality than FBP. [57, 122, 127] However, iterative reconstruction suffers from long computing time due to the large number of iterations with repeated forward and back projection steps. Moreover, in the forward projection step, it requires the knowledge of energy spectrum which is difficult to directly measure.[29, 62, 132, 182] It is usually simplified by a monoenergetic forward projection matrix, or having an indirect simulation/estimation of energy spectrum.[46, 47, 122, 153, 154]

Image synthesis by deep learning seems attractive for low dose CT restoration due to its data-driven approaches toward automatically learning image features and model parameters. As listed in Table VII, most of the methods in the reviewed literatures are direct image translation from low dose CT to full dose CT, while the others restore the sinogram using deep learning first, and then reconstruct images from the restored sonogram by FBP. As shown by Dong *et al.*, with similar network, their proposed projection-based method outperformed an image-based method in better reducing downsampling artifacts with higher resolution on edges of the object.[24] A potential reason of such difference, as comment by the authors, is that for image-based method, the error in prediction is directly shown on image, while for projection-based method, the error predicted on sonogram will be compensated in the reconstruction process which is inherently a weighted sum. Thus projection-based method can be

more tolerant to errors. It is also possible to train the model to map directly from projection domain to image domain, while the network must encode a change between polar and Cartesian coordinates.[61] Among image-domain methods, Shan et al used a progressive scheme that denoised the input low dose CT multiple times and yielded a sequence of denoised images at different noise levels.[138] In the study of Kang *et al.*, instead of directly mapping low and full dose CT images, the proposed method mapped their wavelet coefficient. The benefit of wavelet transform was shown in better structure recovery than direct image mapping.[68]

Compared with iterative reconstruction methods, learning-based methods require less time and no prior knowledge about energy spectrum. For example, as reported by Wang *et al.*, it takes about one minute to generate an entire 3D volume of their denoised low dose CT images on an average personal computer after their model is trained. In contrast, with the same hardware, a compressed-sensing-based iterative method needs one minute in forward and back projecting on a single slice in one iteration. Alternatively, if the forward and back projecting operation is pre-calculated and saved as a sparse matrix, the time shorten to several seconds for each slice in each iteration, but it requires 6.8 GB space in memory to store the matrix. Even so, to reconstruct the entire volume, it still needs several hours. Thus, it is very time and memory-consuming for conventional iterative reconstruction method to be implemented on personal computer, especially when slices thickness is small and FOV on slice-direction is large.[152]

Conventional iterative reconstruction methods were compared with learning-based methods in several studies. For example, total variation (TV) regularization is commonly studied in state-of-the-art compressed sensing-based iterative methods. A common finding is that TV-based methods tend to over-smooth and present patchy texture, while the results by learning-based methods have finer structures preserved and closer to a full dose CT in image texture. [61, 152] Such improvement of learning-based methods is also shown in quantitative metrics of PSNR, etc. The large recovery of image quality with a preserved image texture could be attributed to the learning process that the prediction images always tend to be trained to have a similar image quality and texture as its target images, i.e. full dose CT images. Similarly, Shan *et al.* demonstrated that their proposed learning-based method performed favorably or comparably to three commercially available iterative algorithms in terms of noise suppression and structural fidelity by double-blinded reader study.

Most of the reviewed studies assume the application of their restored full dose CT to be diagnosis. Wang *et al.* evaluated their method in the context of radiation therapy treatment planning.[152] Their motivation is that low dose CT in CT simulation process is attractive for adaptive radiation therapy where multiple re-scanning and re-planning during treatment course is very common. In contrast to the diagnosis CT that pursues high spatial resolution and low-contrast detectability, planning CT requires accurate HU numbers and dose calculation accuracy. Their dosimetry study showed that the average differences of DVH metrics between the synthetic full dose CT and original full dose CT are less than 0.1 Gy ($p>0.05$) when prescribed dose is 21 Gy.

Many of the reviewed studies used the dataset from the AAPM 2016 Low-dose CT Grand Challenge.[115] Although the training and testing scheme may be different among these studies, the results of these studies can still have a fair comparison. However, this low dose CT dataset, along with the dataset in most of the other studies, is simulated from full dose CT by adding Poisson noise or downsampling sinogram, due to the lack of clinical low dose CT data. Exceptions are Yi *et al.* using piglet and Shan *et al.* using real patient low dose CTs.[138, 175] The simulated noise may not fully reflect the noise level and potential artifacts, thus it is of clinical interest to evaluate these methods with physically measured low dose datasets.

Table VII. Summary of studies on synthetic full dose CT from low dose CT.

Network	Projection or image domain	Site, and # of patients in training/testing	Low dose scheme and fraction of full dose CT	Key findings in restored full dose CT	Author, year
U-net	Image	Abdomen: 10 training/20 testing	Low mAs: 1/4 of full dose	PSNR (dB): about 36	Kang <i>et al.</i> , 2017[68]

U-net	Image	Abdomen: 10, leave-one-out	Low mAs: 1/4 of full dose	PSNR (dB): 44.4187±1.211	Chen <i>et al.</i> , 2017[15]
U-net	Image	Thorax and pelvis: 475 slices training/25 slices testing	Sparse view: 1/20 of full views	PSNR (dB): 28.83	Jin <i>et al.</i> , 2017[61]
GAN	Image	Cardiac: 28, 2-fold cross validation	Low mAs: 20% dose	Significantly reduced noise	Wolterink <i>et al.</i> , 2017[162]
CNN(ResNet)	Image	Abdomen: 9 training/1 testing	Low mAs: 1/4 of full dose	PSNR (dB): 39.8329	Yang <i>et al.</i> , 2017[169]
CNN (ResNet)	Image	Abdomen: 8 training/1 testing	Low mAs: 1/4 of full dose	PSNR (dB): 38.70	Kang <i>et al.</i> , 2018[67]
GAN	Image	Abdomen (piglet): 708 slices training/142 slices testing	Low mAs: 5% of full mAs	PSNR (dB): about 34	Yi <i>et al.</i> , 2018[175]
GAN	Image	Abdomen: 5 training/5 testing	Low mAs: 1/4 of full dose	PSNR(dB): 30.137±1.938	Shan <i>et al.</i> , 2018[137]
GAN	Image	Abdomen: 10, leave-one-out	Low mAs: 1/4 of full dose	PSNR (dB): (25.372, 27.398) +	You <i>et al.</i> , 2018[176]
U-net	Image	Abdomen: 8 training/1 validation/1 testing	Sparse view: 1/12 of full views	PSNR (dB): 40.4856	Han <i>et al.</i> , 2018[43]
GAN	Image	Abdomen: 4000 slices training/2000 testing	Low mAs: 1/4 of full dose	Validated in double-blinded reader study	Yang <i>et al.</i> , 2018[168]
U-net (Encoder-decoder)	Image	Whole body: 300 slices training/50 slices testing	Low mAs: fraction not specified	PSNR (dB): 42.3257	Liu <i>et al.</i> , 2018[107]
CNN	Image	Chest: 3 training/3 testing	Low mAs: 3% of full mAs	PSNR (dB): about 22	Zhao <i>et al.</i> , 2019[181]
U-net	Projection	Chest: 7 training/8 testing	Sparse view: 1/4 of full views	PSNR (dB): (42.73, 52.14)	Lee <i>et al.</i> , 2019[86]
U-net	Image	Abdomen and chest: 10 training/60 testing	Low mAs: about 1/3 to 1/8 of full dose	Validated in double-blinded reader study	Shan <i>et al.</i> , 2019[138]
U-net	Projection	Head: 200 slices training/100 slices testing	Sparse view: 1/12 of full views Limited angle: 1/4 of full views	PSNR (dB): 37.21 for sparse view 43.69 for limited angle	Dong <i>et al.</i> , 2019[24]
CycleGAN	Image	Head: 30, 5-fold cross validation	Low mAs: 0.5% of full mAs	NMSE (%): 1.63±0.62	Wang <i>et al.</i> , 2019[152]

[†]Numbers in parentheses indicate minimum and maximum values.

4.2.2 MRI

Image synthesis has been investigated for various applications in MR imaging,[92] such as imaging translation among different sequences, converting low-magnetic-field MRI to high-magnetic-field MRI, and restoring undersampled acquisition. The motivation of converting a low-magnetic-field MRI to high-magnetic-field MRI is to acquire MR images by an accessible MRI scanner but with high spatial resolution and good contrast as on a cutting-edge scanner. The translation among different sequences and restoring undersampled acquisition can both shorten the acquisition time. The challenges in the former are mapping the different contrast, and in the latter are recovering the spatial resolution. Although these applications are not exactly the same in terms, they pose similar problems for image synthesis, i.e. preserving contrast and resolution.

A large group of conventional methods that address these problems are compressed sensing methods assuming that images have a sparse representation in some transform domain. For example, in image synthesis among multi-contrast MRI, the image patch of one contrast is expressed as a sparse linear combination of patches in atlas, and such combination is then applied on the image patches on the other contrast. In recovering undersampled acquisition, the problem is usually modeled as a reconstruction problem with regularization terms that incorporate prior knowledge about the sparsity of images. It is usually implemented as an iterative algorithm to solve the optimization problem, which is time and resource intensive. Another property of CS is that it requires incoherence in the sampling scheme, which can be disadvantageous in some cases such as when downsampling in k-space region is preferable.[74] On the other hand, the success of deep learning in other imaging synthesis fields encourages the integration of neural network into the above situations for its favorable performance in short prediction time as well as non-linear mapping capability.

The related studies are listed in Table VIII. Compared with image synthesis in other applications, more reviewed studies of MR inter-modality incorporate neural network with other techniques, rather than a direct end-to-end method. It is also common to apply neural network in transform domains. Zhang *et al.* proposed a cascaded regression using two parallel and interactive multi-layer network streams on spatial and frequency domains. Compared with using single spatial-domain, the dual-domain method presented better visual results and significantly larger SSIM.[180] Qu *et al.* designed a wavelet-based affine transformation layer to modulate feature maps from spatial domain and wavelet domain in the encoder, followed by the image reconstruction decoder branch that synthesizes 7T images from the wavelet modulated spatial information. Without such layer, the framework was reduced to a plain encoder-decoder network, which was found to be less capable in recovering details.[130]

Many of the reviewed studies also compared their proposed method with CS-based method. With a comparable or better performance on quantitative image quality metrics, a noticeable improvement is much less computational time. The predication of learning-based method is usually in a magnitude of millisecond to second, while CS-based method is in minutes. Schlemper *et al.* found that at low undersampling rate, learning-based and CS-based methods had comparable performance, and the advantageous performance of learning-based method was shown at more aggressive undersampling factor.[135] Other findings of blurred details and blocky artifacts as mentioned in previous sections were also reported.

Table VIII. Summary of studies on synthetic MRI.

Network	Applications	Site, and # of patients in training/testing	Key findings in results	Author, year
GAN	Synthesizing 7T MRI from 3T MRI	Brain: 15, leave-one-out	PSNR (dB): 27.6±1.3	Nie <i>et al.</i> , 2018[120]
CNN	Restoring undersampled acquisition	Cardiac: 5 training/5 testing	Restored images showed most of the anatomical structures up to 11-fold undersampling	Schlemper <i>et al.</i> , 2018[135]

GAN	Low resolution to high resolution	Brain: 196 training/48 testing	SSIM: (0.76, 0.94) ⁺ at 8-fold undersampling	Kim <i>et al.</i> , 2018[74]
U-net	Synthesizing full contrast enhanced images from low contrast enhanced images	Brain: 10 training/50 testing	PSNR (dB): 28.07±2.26 at 10-fold lower	Gong <i>et al.</i> , 2018[37]
U-net	T1w to T2w T1w to FLAIR PDw to T2w	Three different brain datasets: 22 training/3 validation/3 testing 42 training/6 validation/6 testing 22 training/3 validation/3 testing	Average PSNR (dB) among groups of datasets: (25.78, 32.92) for synthetic T2w (29.99, 30.32) for synthetic FLAIR	Chartsias <i>et al.</i> , 2018[14]
GAN	Restoring under-sampled acquisition	Brain and chest: for each site, 100 slices training/100 slices testing	PSNR (dB) at 10% undersampling: about 32 for brain, 26.5 for chest	Quan <i>et al.</i> , 2018[131]
GAN	Low resolution to high resolution T1w to T2w T2w to T1w T2w to STIR T2w to TIRM	767 training/192 validation/30 testing 767 training/192 validation/30 testing 767 training/192 validation/30 testing 284 training/71 validation/30 testing 305 training/77 validation/30 testing	Average PSNR (dB): about (25, 30)	Galbusera <i>et al.</i> , 2018[36]
GAN	T1w to T2w T2w to T1w	Brain: 3 datasets, 48 training/5 validation/13 testing, 25 training/5 validation/10 testing, 24 training/2 validation/15 testing	Average PSNR (dB): (25.80±1.87, 29.77±1.57) among three datasets	Dar <i>et al.</i> , 2019[20]
GAN	Restoring under-sampled acquisition	Abdomen: 336 training/10 testing	SSIM: 0.84 at 5-fold undersampling	Mardani <i>et al.</i> , 2019[113]
U-net	Synthesizing DTI from fMRI	Brain: 648 training/293 testing	Mean correlation coefficient: 0.808±0.054 among 38 VOIs	Son <i>et al.</i> , 2019[143]
CNN	Synthesizing FLAIR from mpMRI	Brain: 24, 5-fold cross validation	SSIM: 0.860±0.031	Wei <i>et al.</i> , 2019[161]
GAN	Synthesizing diffusion b0 maps from T1w	Brain: 586 training/26 testing	Distortion correction based on synthesized b0 maps is feasible	Schilling <i>et al.</i> , 2019[134]

CNN (ResNet)	Synthesizing arterial spin labeling images from T1w	Brain: 355, 5-fold cross validation	Accuracy in CBF calculation and dementia disease diagnosis is close to gold standard	Huang <i>et al.</i> , 2019[52]
CNN	Synthesizing 7T MRI from 3T MRI	Brain: 15, leave-one-out	SSIM: 0.8438	Zhang <i>et al.</i> , 2019[180]
U-net	Restoring under-sampled acquisition	Knee: 90 training/10 validation/10 testing	SSIM: 0.821±0.023 at 8-fold under-sampling	Liu <i>et al.</i> , 2019[102]
U-net (encoder-decoder)	Synthesizing 7T MRI from 3T MRI	Brain: 15, leave-one-out	PSNR (dB): 28.27	Qu <i>et al.</i> , 2020[130]
U-net	Restoring under-sampled acquisition	Knee: 336 training/24 testing	SSIM: 0.8603 at 4-fold undersampling	Wu <i>et al.</i> , 2020[163]
U-net	Synthesizing MR angiography from 3D-QALAS sequence	Brain: 11, 5-fold cross validation	PSNR (dB): 35.3±0.5	Fujita <i>et al.</i> , 2020[35]

⁺Numbers in parentheses indicate minimum and maximum values.

4.2.3 PET

Image synthesis among different PET images has been proposed to facilitate PET AC and low-count PET reconstruction. For the PET AC, unlike what is mentioned in section 4.1.4 that synthetic CT is generated from NAC PET for attenuation correction during PET reconstruction, a few studies, as listed in Table IX, investigated the feasibility of direct mapping NAC PET to AC PET by exploiting the deep learning methods to bypass the PET reconstruction step. These studies reported comparable results with synthetic CT-based PET AC (section 4.1.4), while a direct comparison on same datasets were not found. Dong *et al.* applied the direct NAC PET-AC PET mapping on whole body for the first time.[26] They also demonstrate the reliability of their method by including sequential scans in their testing datasets to evaluate the PET intensity changes with time on their AC PET as well as ground truth. Similar as their study using synthetic CT, lung showed the largest error. Shiri *et al.* further assessed the radiomic features on their AC PET results, and found only 3 out of 83 regions had significant difference with ground truth.[139]

Low-count PET has extensive application in pediatric PET scan and radiotherapy response evaluation with advantage of better motion control and low patient dose. However, the low count statistics would result in increased image noise, reduced contrast-to-noise ratio, and large bias in uptake measurement. The reconstruction of a standard- or full-count PET from the low-count PET cannot be achieved by simple postprocessing operations such as denoising since lowering radiation dose changes the underlying biological and metabolic process, leading to not only noise but also local uptake values changes.[85] Moreover, even with a same tracer injection dose, the uptake distribution and signal level can vary greatly among patients. The learning-based low-count PET reconstruction methods, as summarized in Table X, have been proposed to take advantage of their powerful data-driven feature extraction capabilities between two image datasets. A few of the reviewed methods used both MR and low-count PET as input, while most used low-count PET only. Most proposed methods were implemented on PET brain scans, with a few on lung and whole body. Compared with the evaluations in PET AC which focus on relative bias, the evaluations in the reviewed studies in low-count PET reconstruction more focus on the image quality and the similarity between the predicted result and its corresponding full-count PET ground truth.

Similar as low dose CT restoration, most low-count PET restoration studies applied neural network directly on image domain, with a few on projection domain. In addition to the advantages mentioned in section 4.2.1, Sanaat *et al.* commented that projection-based network allows the change of reconstruction filter or any post-processing without the need of retrain the model.[133] They also compared the

results by the same proposed network using image and projection as input, and found that projection-based results better reflected uptake pattern and anatomy than image-based results, and both subjective and objective studies validated the advantages of projection-based results. A drawback of projection-based method is six times longer training time than image-based method.

Although these studies demonstrate the feasibility of mapping low-count PET to full-count PET, a few studies investigated using both PET and MRI image as dual input channels to further improve the results when MR images are available. As expected, the addition of MRIs that provides anatomical information could help improve the performance of the network than without MR. Chen *et al.* showed that their network is able to achieve 83% accuracy when using only PET as input, and 89% when using PET+MR, in a clinical reading study of uptake status.[16] The potential reason of such difference lies in that the results by PET+MR were superior in reflecting the underlying anatomic patterns. The contribution of MR images was also validated in the study of Xiang et al by a significant improved PSNR.[164] They commented that structural information from MRIs yields important cues for estimating the high-quality PET, even though structural MRIs differ from PETs significantly regarding their appearances.

Table IX. Summary of studies on synthetic AC PET from NAC PET.

Network	Site, and # of patients in training/testing	Key findings in PET quality	Author, year
U-net	Brain: 25 training/10 testing	Bias (%): 4.0 ± 15.4	Yang <i>et al.</i> , 2019[167]
U-net	Brain: 91 training/18 testing	Bias (%): -0.10 ± 2.14 among 83 VOIs	Shiri <i>et al.</i> , 2019[139]
CycleGAN	Whole body: 25 training/10 patients*3 sequential scan testing	Bias (%): $(-17.02, 3.02)^+$ among 6 VOIs, 2.85 ± 5.21 in lesions	Dong <i>et al.</i> , 2019[26]

⁺Numbers in parentheses indicate minimum and maximum values.

Table X. Summary of studies on synthetic full count PET from low count PET.

Network	PET or PET+MR	Image or projection domain	Site, and # of patients in training/testing	Counting fraction (low/full)	Key findings in restored full counting PET	Author, year
CNN	PET+MR	Image	Brain: 16, leave-one-out	1/4	PSNR (dB): 24.76	Xiang <i>et al.</i> , 2017[164]
GAN	PET	Image	Brain: 16, leave-one-out	1/4	PSNR (dB): about 24	Wang <i>et al.</i> , 2018[157]
U-net	PET+MR	Image	Brain: 40, five-fold cross-validation	1/100	PSNR (dB): about 38	Chen <i>et al.</i> , 2019[16]
CNN	PET	Image	Brain: 2 training/1 testing Lung: 5 training/1 testing	Brain: 1/5 Lung: 1/10	N/A	Gong <i>et al.</i> , 2019[38]
U-net (encoder-decoder)	PET	Projection	Whole body (simulation): 245 training/52 validation/53 testing	N/A	PSNR (dB): 34.69	Hägström <i>et al.</i> , 2019[41]
GAN	PET+MR	Image	Brain: 16, leave-one-out	?	PSNR (dB): 24.61	Wang <i>et al.</i> , 2019[159]

GAN	PET	Image	Brain: 40, four-fold cross validation	1/100	PSNR (dB): about 30	Ouyang <i>et al.</i> , 2019[126]
U-net	PET	Image	Lung: 10, five-fold cross validation	1/10	Bias: <15%	Lu <i>et al.</i> , 2019[110]
GAN	PET	Image	Whole body: 435 slices training/440 slices testing	1/10	PSNR (dB): 30.557	Kaplan <i>et al.</i> , 2019[69]
CycleGAN	PET	Image	Whole body: 25 training/10 testing	1/8	PSNR (dB): 41.5±2.5	Lei <i>et al.</i> , 2019[89]
U-net	PET	Projection	Brain: 100 training/20 validation/20 testing	1/20	PSNR (dB): 38.25±0.66	Sanaat <i>et al.</i> , 2020[133]

5 SUMMARY AND OUTLOOK

Recent years have witnessed the trend of deep learning being increasingly used in the application of medical imaging. The latest networks and techniques have been borrowed from computer vision field and adapted to specific clinical tasks for radiology and radiation oncology. As reviewed in this paper, learning-based image synthesis is an emerging and active field since all of these reviewed studies were published within the recent three years. With the development in both artificial intelligence and computing hardware, more learning-based methods are expected to facilitate the clinical workflow with novel applications. Although the reviewed literatures show the success of deep learning-based image synthesis in various applications, there are still some common open questions that need to be answered in future studies.

In the implementation of the network, due to the imitations of the GPU memory, some of the deep learning approaches are trained on two-dimensional (2D) slices. Since the loss functions of 2D models do not account for continuity in the third dimension, slice discontinuities can be observed. Some studies trained models in 3D patches to exploit 3D information with even less memory burden,[90] while a potential drawback is that the larger scale image features may be hard to extract.[22] Training on three-dimensional (3D) image stacks is expected to achieve a more homogeneous conversion result. Fu *et al.* compared the performance between 2D and 3D model using the same U-net.[34] They found that 3D model generated synthetic CT with smaller MAE and more accurate bone region. However, to achieve robust performance, 3D model needs more training data since it has more parameters. A compromised solution is to use multiple adjacent slices that may allow the model to capture more image context information, or to train different networks for all three orthogonal 2D planes to allow pseudo 3D information.[134]

The reviewed studies showed the advantages of learning-based methods over conventional methods in performance as well as clinical applications. Learning-based methods generally outperform conventional methods in generating more realistic synthetic images with higher similarity to real images and better quantitative metrics. In implementation, depending on the hardware, training a model usually takes several hours to days for learning-based methods. However, once the model is trained, it can be applied to new patients to generate synthetic images within a few seconds or minutes. Conventional methods vary a lot in specific methodologies and implementations, resulting in a wide range of run time. Iterative methods such as CS were shown to be unfavorable for large time and resource consuming.

In the training stage, most of the reviewed studies require paired datasets, i.e. the source image and target image need to have pixel-to-pixel correspondence. This requirement poses difficulties in collecting sufficient eligible datasets, as well as demands high accuracy in image registration. Some networks

such as CycleGAN can relax the requirement of the paired datasets to be unpaired datasets, which can be beneficial for clinical application in enrolling large number of patient datasets for training.

Although the advantages of learning-based methods have been demonstrated, it should be noted that its performance can be unpredictable when the input images are very different from its training datasets. In most of the reviewed studies, unusual cases are excluded. However, these unusual cases can happen from time to time in clinic, and should be dealt with caution. For example, it is not uncommon to see patient with hip prosthesis in pelvis scan. The hip prosthesis creates severe artifacts on both CT and MR images, thus, it can be of clinical interest to see the related effect of its inclusion in training or testing dataset, which has not been studied yet. Similar unusual cases can also be seen in other forms in all imaging modalities and are worth investigation, including all kinds of implants that can introduce artifacts, obese patients that present much higher noise level on image than average, and patients with anatomical abnormality.

Due to the limitation in the number of available datasets, most studies used N-fold cross validation or leave-N-out strategy. The small to intermediate number of patients in training/testing is proper for feasibility study, while is far from enough in evaluating clinical utility and potential impact. Moreover, the representativeness of training/testing dataset needs special attention in clinical study. The missing of diverse demographics may reduce the robustness and generality in the performance of the model. Most of the studies trained model using data from a single institution with a single scanner. As replacing/equipping with new scanner is common in practice, it is interesting to know how the trained model would perform on another scanner of different model or vendor when the image characteristic cannot be exactly matched. Boni *et al.* recently presented a proof-of-concept study that predicted synthetic images of one site using model trained on another two sites, and demonstrated the clinical acceptable synthetic results.[12] Further studies could include datasets from multiple centers and adopted a leave-one-center-out training/test strategy in order to validate the consistency and robustness of the network.

Before being deployed into clinical workflow, there are still a few challenges to be addressed. To account for the potential unpredictable synthetic images that can be resulted by noncompliance with imaging protocols as training data, or unexpected anatomic structures, additional quality assurance (QA) step would be essential in clinical practice. The QA procedure would aim to check the consistency on the performance of the model routinely or after upgrade by re-training the network with more patient datasets, as well as to check the synthetic image quality of patient-specific case.

6 ACKNOWLEDGEMENT

This research was supported in part by the National Cancer Institute of the National Institutes of Health under Award Number R01CA215718 and Emory Winship Cancer Institute pilot grant.

References

- [1] November 01, 2016 2016. URL <https://ui.adsabs.harvard.edu/abs/2016arXiv161107004I>.
- [2] Zerda Adam de la, Armbruster Benjamin, and Xing Lei. Formulating adaptive radiation therapy (art) treatment planning into a closed-loop control framework. *Physics in Medicine & Biology*, 52(14):4137, 2007. ISSN 0031-9155. URL <http://stacks.iop.org/0031-9155/52/i=14/a=008>.
- [3] Thummerer Adrian, Zaffino Paolo, Meijers Arturs, G. Marmitt Gabriel, Seco Joao, J. H. M. Steenbakkens Roel, A. Langendijk Johannes, Both Stefan, Spadea Maria Francesca, and Knopf Antje-Christin. Comparison of cbct based synthetic ct methods suitable for proton dose calculations in adaptive proton therapy. *Physics in Medicine & Biology*, 2020. ISSN 0031-9155. URL <http://iopscience.iop.org/10.1088/1361-6560/ab7d54>.
- [4] H. Arabi, J. A. Dowling, N. Burgos, X. Han, P. B. Greer, N. Koutsouvelis, and H. Zaidi. Comparative study of algorithms for synthetic ct generation from mri: Consequences for mri-guided radiation planning in the pelvic region. *Medical Physics*, 45(11):5218–5233, 2018. ISSN 0094-2405. doi: 10.1002/mp.13187.

- [5] H. Arabi, G. Zeng, G. Zheng, and H. Zaidi. Novel adversarial semantic structure deep learning for mri-guided attenuation correction in brain pet/mri. *European Journal of Nuclear Medicine and Molecular Imaging*, 46(13):2746–2759, 2019. ISSN 1619-7070. doi: 10.1007/s00259-019-04380-x.
- [6] K. Armanious, T. Kustner, M. Reimold, K. Nikolaou, C. La Fougere, B. Yang, and S. Gatidis. Independent brain (18)f-fdg pet attenuation correction using a deep learning approach with generative adversarial networks. *Hellenic Journal of Nuclear Medicine*, 22(3):179–186, 2019. ISSN 1790-5427 (Print) 1790-5427. doi: 10.1967/s002449911053.
- [7] Brandon M. Barney, R. Jeffrey Lee, Diana Handrahan, Keith T. Welsh, J. Taylor Cook, and William T. Sause. Image-guided radiotherapy (igrt) for prostate cancer comparing kv imaging of fiducial markers with cone beam computed tomography (cbct). *International Journal of Radiation Oncology*Biophysics*, 80(1):301–305, 2011. ISSN 0360-3016. doi: 10.1016/j.ijrobp.2010.06.007. URL <http://dx.doi.org/10.1016/j.ijrobp.2010.06.007>.
- [8] Paul Blanc-Durand, Maya Khalife, Brian Sgard, Sandeep Kaushik, Marine Soret, Amal Tiss, Georges El Fakhri, Marie-Odile Habert, Florian Wiesinger, and Aurlie Kas. Attenuation correction using 3d deep convolutional neural network for brain 18f-fdg pet/mr: Comparison with atlas, zte and ct based attenuation correction. *PLoS One*, 14(10):e0223141, 2019. doi: 10.1371/journal.pone.0223141. URL <https://doi.org/10.1371/journal.pone.0223141>.
- [9] John M. Boone and J. Anthony Seibert. An analytical model of the scattered radiation distribution in diagnostic radiology. *Medical Physics*, 15(5):721–725, 1988. doi: doi:http://dx.doi.org/10.1118/1.596186. URL <http://scitation.aip.org/content/aapm/journal/medphys/15/5/10.1118/1.596186>.
- [10] D. Brenner, C. Elliston, E. Hall, and W. Berdon. Estimated risks of radiation-induced fatal cancer from pediatric ct. *American Journal of Roentgenology*, 176(2):289–96, 2001. ISSN 0361-803X (Print) 0361-803x. doi: 10.2214/ajr.176.2.1760289.
- [11] David J. Brenner and Eric J. Hall. Computed tomography an increasing source of radiation exposure. *New England Journal of Medicine*, 357(22):2277–2284, 2007. doi: doi:10.1056/NEJMra072149. URL <http://www.nejm.org/doi/fu11/10.1056/NEJMra072149>.
- [12] Kvin N. D. Brou Boni, John Klein, Ludovic Vanquin, Antoine Wagner, Thomas Lacornerie, David Pasquier, and Nick Reynaert. Mr to ct synthesis with multicenter data in the pelvic area using a conditional generative adversarial network. *Physics in Medicine & Biology*, 65(7):075002, 2020. ISSN 1361-6560. doi: 10.1088/1361-6560/ab7633. URL <http://dx.doi.org/10.1088/1361-6560/ab7633>.
- [13] C. Burger, G. Goerres, S. Schoenes, A. Buck, A. H. Lonn, and G. K. Von Schulthess. Pet attenuation coefficients from ct images: experimental evaluation of the transformation of ct into pet 511-kev attenuation coefficients. *European Journal of Nuclear Medicine and Molecular Imaging*, 29(7):922–7, 2002. ISSN 1619-7070 (Print) 1619-7070. doi: 10.1007/s00259-002-0796-3.
- [14] A. Chartsias, T. Joyce, M. V. Giuffrida, and S. A. Tsiftaris. Multimodal mr synthesis via modality-invariant latent representation. *IEEE Transactions on Medical Imaging*, 37(3):803–814, 2018. ISSN 1558-254X. doi: 10.1109/TMI.2017.2764326.
- [15] H. Chen, Y. Zhang, M. K. Kalra, F. Lin, Y. Chen, P. Liao, J. Zhou, and G. Wang. Low-dose ct with a residual encoder-decoder convolutional neural network. *IEEE Transactions on Medical Imaging*, 36(12):2524–2535, 2017. ISSN 0278-0062. doi: 10.1109/tmi.2017.2715284.
- [16] K. T. Chen, E. Gong, F. B. de Carvalho Macruz, J. Xu, A. Boumis, M. Khalighi, K. L. Poston, S. J. Sha, M. D. Greicius, E. Mormino, J. M. Pauly, S. Srinivas, and G. Zaharchuk. Ultra-low-dose (18)f-florbetaben amyloid pet imaging using deep learning with multi-contrast mri inputs. *Radiology*, 290(3):649–656, 2019. ISSN 0033-8419. doi: 10.1148/radiol.2018180940.
- [17] L. Chen, X. Liang, C. Shen, S. Jiang, and J. Wang. Synthetic ct generation from cbct images via deep learning. *Medical Physics*, 2019. ISSN 0094-2405. doi: 10.1002/mp.13978.

- [18] S. Chen, A. Qin, D. Zhou, and D. Yan. Technical note: U-net-generated synthetic ct images for magnetic resonance imaging-only prostate intensity-modulated radiation therapy treatment planning. *Medical Physics*, 45(12):5659–5665, 2018. ISSN 0094-2405. doi: 10.1002/mp.13247.
- [19] A. P. Colijn and F. J. Beekman. Accelerated simulation of cone beam x-ray scatter projections. *IEEE Transactions on Medical Imaging*, 23(5):584–90, 2004. ISSN 0278-0062 (Print) 0278-0062.
- [20] S. U. Dar, M. Yurt, L. Karacan, A. Erdem, E. Erdem, and T. ?ukur. Image synthesis in multi-contrast mri with conditional generative adversarial networks. *IEEE Transactions on Medical Imaging*, 38(10):2375–2388, 2019. ISSN 1558-254X. doi: 10.1109/TMI.2019.2901750.
- [21] Slobodan Devic. Mri simulation for radiotherapy treatment planning. *Medical Physics*, 39(11):6701–6711, 2012. ISSN 2473-4209. doi: 10.1118/1.4758068. URL <http://dx.doi.org/10.1118/1.4758068>.
- [22] A. M. Dinkla, M. C. Florkow, M. Maspero, M. H. F. Savenije, F. Zijlstra, P. A. H. Doornaert, M. van Stralen, M. E. P. Philippens, C. A. T. van den Berg, and P. R. Seevinck. Dosimetric evaluation of synthetic ct for head and neck radiotherapy generated by a patch-based three-dimensional convolutional neural network. *Medical Physics*, 46(9):4095–4104, 2019. ISSN 0094-2405. doi: 10.1002/mp.13663.
- [23] Anna M. Dinkla, Jelmer M. Wolterink, Matteo Maspero, Mark H. F. Savenije, Joost J. C. Verhoeff, Enrica Seravalli, Ivana I?gum, Peter R. Seevinck, and Cornelis A. T. van den Berg. Mr-only brain radiation therapy: Dosimetric evaluation of synthetic cts generated by a dilated convolutional neural network. *International Journal of Radiation Oncology*Biolog*Physics*, 102(4):801–812, 2018. ISSN 0360-3016. doi: <https://doi.org/10.1016/j.ijrobp.2018.05.058>. URL <http://www.sciencedirect.com/science/article/pii/S0360301618309106>.
- [24] J. Dong, J. Fu, and Z. He. A deep learning reconstruction framework for x-ray computed tomography with incomplete data. *PLoS One*, 14(11):e0224426, 2019. ISSN 1932-6203. doi: 10.1371/journal.pone.0224426.
- [25] X. Dong, Y. Lei, S. Tian, Tonghe Wang, P. Patel, W. J. Curran, A. B. Jani, T. Liu, and Xiaofeng Yang. Synthetic mri-aided multi-organ segmentation on male pelvic ct using cycle consistent deep attention network. *Radiotherapy and Oncology*, 141:192–199, 2019. ISSN 0167-8140. doi: 10.1016/j.radonc.2019.09.028.
- [26] X. Dong, Y. Lei, T. Wang, K. Higgins, T. Liu, W. J. Curran, H. Mao, J. A. Nye, and X. Yang. Deep learning-based attenuation correction in the absence of structural information for whole-body pet imaging. *Physics in Medicine & Biology*, 2019. ISSN 0031-9155. doi: 10.1088/1361-6560/ab652c.
- [27] X. Dong, Tonghe Wang, Y. Lei, K. Higgins, T. Liu, W. J. Curran, H. Mao, J. A. Nye, and Xiaofeng Yang. Synthetic ct generation from non-attenuation corrected pet images for whole-body pet imaging. *Physics in Medicine & Biology*, 64(21):215016, 2019. ISSN 0031-9155. doi: 10.1088/1361-6560/ab4eb7.
- [28] Jason A. Dowling, Jonathan Lambert, Joel Parker, Olivier Salvado, Jurgen Fripp, Anne Capp, Chris Wratten, James W. Denham, and Peter B. Greer. An atlas-based electron density mapping method for magnetic resonance imaging (mri)-alone treatment planning and adaptive mri-based prostate radiation therapy. *International Journal of Radiation Oncology*Biolog*Physics*, 83(1):e5–e11, 2012. ISSN 0360-3016. doi: <https://doi.org/10.1016/j.ijrobp.2011.11.056>. URL <http://www.sciencedirect.com/science/article/pii/S0360301611036145>.
- [29] I. A. Elbakri and J. A. Fessler. Statistical image reconstruction for polyenergetic x-ray computed tomography. *IEEE Transactions on Medical Imaging*, 21(2):89–99, 2002. ISSN 0278-0062. doi: 10.1109/42.993128.
- [30] H. Emami, M. Dong, S. P. Nejad-Davarani, and C. K. Glide-Hurst. Generating synthetic cts from magnetic resonance images using generative adversarial networks. *Medical Physics*, 2018. ISSN 0094-2405. doi: 10.1002/mp.13047.

- [31] B. G. Fallone, B. Murray, S. Rathee, T. Stanescu, S. Steciw, S. Vidakovic, E. Blosser, and D. Tymofichuk. First mr images obtained during megavoltage photon irradiation from a prototype integrated linac-mr system. *Medical Physics*, 36(6Part1):2084–2088, 2009. ISSN 2473-4209. doi: 10.1118/1.3125662. URL <http://dx.doi.org/10.1118/1.3125662>.
- [32] M. C. Florkow, F. Zijlstra, K. Willemsen, M. Maspero, C. A. T. van den Berg, L. G. W. Kerkmeijer, R. M. Castelein, H. Weinans, M. A. Viergever, M. van Stralen, and P. R. Seevinck. Deep learning-based mr-to-ct synthesis: The influence of varying gradient echo-based mr images as input channels. *Magnetic resonance in Medicine*, 83(4):1429–1441, 2020. ISSN 0740-3194. doi: 10.1002/mrm.28008.
- [33] M. T. Freitag, M. Fenchel, P. Baumer, T. Heusser, C. M. Rank, M. Kachelriess, D. Paech, K. Kopka, S. Bickelhaupt, A. Dimitrakopoulou-Strauss, K. Maier-Hein, R. Floca, M. E. Ladd, H. P. Schlemmer, and F. Maier. Improved clinical workflow for simultaneous whole-body pet/mri using high-resolution caipirinha-accelerated mr-based attenuation correction. *European Journal of Radiology*, 96:12–20, 2017. ISSN 0720-048x. doi: 10.1016/j.ejrad.2017.09.007.
- [34] J. Fu, Y. Yang, K. Singhrao, D. Ruan, F. I. Chu, D. A. Low, and J. H. Lewis. Deep learning approaches using 2d and 3d convolutional neural networks for generating male pelvic synthetic computed tomography from magnetic resonance imaging. *Medical Physics*, 46(9):3788–3798, 2019. ISSN 0094-2405. doi: 10.1002/mp.13672.
- [35] S. Fujita, A. Hagiwara, Y. Otsuka, M. Hori, N. Takei, K. P. Hwang, R. Irie, C. Andica, K. Kamagata, T. Akashi, K. Kunishima Kumamaru, M. Suzuki, A. Wada, O. Abe, and S. Aoki. Deep learning approach for generating mra images from 3d quantitative synthetic mri without additional scans. *Investigative Radiology*, 2020. ISSN 0020-9996. doi: 10.1097/rli.0000000000000628.
- [36] F. Galbusera, T. Bassani, G. Casaroli, S. Gitto, E. Zanchetta, F. Costa, and L. M. Sconfienza. Generative models: an upcoming innovation in musculoskeletal radiology? a preliminary test in spine imaging. *European Radiology Experimental*, 2(1):29, 2018. ISSN 2509-9280. doi: 10.1186/s41747-018-0060-7.
- [37] E. Gong, J. M. Pauly, M. Wintermark, and G. Zaharchuk. Deep learning enables reduced gadolinium dose for contrast-enhanced brain mri. *Journal of Magnetic Resonance Imaging*, 48(2):330–340, 2018. ISSN 1053-1807. doi: 10.1002/jmri.25970.
- [38] K. Gong, J. Guan, C. Liu, and J. Qi. Pet image denoising using a deep neural network through fine tuning. *IEEE Transactions on Radiation and Plasma Medical Sciences*, 3(2):153–161, 2019. ISSN 2469-7303. doi: 10.1109/TRPMS.2018.2877644.
- [39] Kuang Gong, Jaewon Yang, Kyungsang Kim, Georges El Fakhri, Youngho Seo, and Quanzheng Li. Attenuation correction for brain pet imaging using deep neural network based on dixon and zte mr images. *Physics in Medicine & Biology*, 63(12):125011, 2018. ISSN 1361-6560. doi: 10.1088/1361-6560/aac763. URL <http://dx.doi.org/10.1088/1361-6560/aac763>.
- [40] D. Gupta, M. Kim, K. A. Vineberg, and J. M. Balter. Generation of synthetic ct images from mri for treatment planning and patient positioning using a 3-channel u-net trained on sagittal images. *Frontiers in Oncology*, 9:964, 2019. ISSN 2234-943X (Print) 2234-943x. doi: 10.3389/fonc.2019.00964.
- [41] I. Haggstrom, C. R. Schmidlein, G. Campanella, and T. J. Fuchs. DeepPET: A deep encoder-decoder network for directly solving the pet image reconstruction inverse problem. *Medical Image Analysis*, 54:253–262, 2019. ISSN 1361-8415. doi: 10.1016/j.media.2019.03.013.
- [42] X. Han. Mr-based synthetic ct generation using a deep convolutional neural network method. *Medical Physics*, 44(4):1408–1419, 2017. ISSN 0094-2405. doi: 10.1002/mp.12155.
- [43] Y. Han and J. C. Ye. Framing u-net via deep convolutional framelets: Application to sparse-view ct. *IEEE Transactions on Medical Imaging*, 37(6):1418–1429, 2018. ISSN 1558-254X. doi: 10.1109/TMI.2018.2823768.

- [44] David C. Hansen, Guillaume Landry, Florian Kamp, Minglun Li, Claus Belka, Katia Parodi, and Christopher Kurz. Scatternet: A convolutional neural network for cone-beam ct intensity correction. *Medical Physics*, 45(11):4916–4926, 2018. ISSN 0094-2405. doi: 10.1002/mp.13175. URL <https://aapm.onlinelibrary.wiley.com/doi/abs/10.1002/mp.13175>.
- [45] J. Harms, Y. Lei, Tonghe Wang, R. Zhang, J. Zhou, X. Tang, W. J. Curran, T. Liu, and Xiaofeng Yang. Paired cycle-gan-based image correction for quantitative cone-beam computed tomography. *Medical Physics*, 46(9):3998–4009, 2019. ISSN 0094-2405. doi: 10.1002/mp.13656.
- [46] Joe Harms, Tonghe Wang, Michael Petrongolo, and Lei Zhu. Noise suppression for energy-resolved ct using similarity-based non-local filtration. In *SPIE Medical Imaging*, volume 9783, page 8. SPIE.
- [47] Joseph Harms, Tonghe Wang, Michael Petrongolo, Tianye Niu, and Lei Zhu. Noise suppression for dual-energy ct via penalized weighted least-square optimization with similarity-based regularization. *Medical Physics*, 43(5):2676–2686, 2016. doi: doi:http://dx.doi.org/10.1118/1.4947485. URL <http://scitation.aip.org/content/aapm/journal/medphys/43/5/10.1118/1.4947485>.
- [48] Joseph Harms, Yang Lei, Tonghe Wang, Rongxiao Zhang, Jun Zhou, Xiangyang Tang, Walter J Curran, Tian Liu, and Xiaofeng Yang. Paired cycleganbased image correction for quantitative conebeam computed tomography. *Medical physics*, 46(9):3998–4009, 2019. ISSN 0094-2405.
- [49] M. Hofmann, F. Steinke, V. Scheel, G. Charpiat, J. Farquhar, P. Aschoff, M. Brady, B. Scholkopf, and B. J. Pichler. Mri-based attenuation correction for pet/mri: a novel approach combining pattern recognition and atlas registration. *Journal of Nuclear Medicine*, 49(11):1875–83, 2008. ISSN 0161-5505 (Print) 0161-5505. doi: 10.2967/jnumed.107.049353.
- [50] Jidong Hou, Mariana Guerrero, Wenjuan Chen, and Warren D. D’Souza. Deformable planning ct to cone-beam ct image registration in head-and-neck cancer. *Medical Physics*, 38(4):2088–2094, 2011. ISSN 2473-4209. doi: 10.1118/1.3554647. URL <http://dx.doi.org/10.1118/1.3554647>.
- [51] Shu-Hui Hsu, Yue Cao, Ke Huang, Mary Feng, and James M. Balter. Investigation of a method for generating synthetic ct models from mri scans of the head and neck for radiation therapy. *Physics in Medicine & Biology*, 58(23):8419, 2013. ISSN 0031-9155. URL <http://stacks.iop.org/0031-9155/58/i=23/a=8419>.
- [52] W. Huang, M. Luo, X. Liu, P. Zhang, H. Ding, W. Xue, and D. Ni. Arterial spin labeling images synthesis from smri using unbalanced deep discriminant learning. *IEEE Transactions on Medical Imaging*, 38(10):2338–2351, 2019. ISSN 0278-0062. doi: 10.1109/tmi.2019.2906677.
- [53] D. Hwang, K. Y. Kim, S. K. Kang, S. Seo, J. C. Paeng, D. S. Lee, and J. S. Lee. Improving the accuracy of simultaneously reconstructed activity and attenuation maps using deep learning. *Journal of Nuclear Medicine*, 59(10):1624–1629, 2018. ISSN 0161-5505. doi: 10.2967/jnumed.117.202317.
- [54] Donghwi Hwang, Seung Kwan Kang, Kyeong Yun Kim, Seongho Seo, Jin Chul Paeng, Dong Soo Lee, and Jae Sung Lee. Generation of pet attenuation map for whole-body time-of-flight 18f-fdg pet/mri using a deep neural network trained with simultaneously reconstructed activity and attenuation maps. *Journal of Nuclear Medicine*, 60(8):1183–1189, 2019. doi: 10.2967/jnumed.118.219493. URL <http://jnm.snmjournals.org/content/60/8/1183.abstract>.
- [55] David Izquierdo-Garcia, Adam E. Hansen, Stefan F?rster, Didier Benoit, Sylvia Schachoff, Sebastian Frst, Kevin T. Chen, Daniel B. Chonde, and Ciprian Catana. An spm8-based approach for attenuation correction combining segmentation and nonrigid template formation: Application to simultaneous pet/mr brain imaging. *Journal of Nuclear Medicine*, 55(11):1825–1830, 2014. doi: 10.2967/jnumed.113.136341. URL <http://jnm.snmjournals.org/content/55/11/1825.abstract>.
- [56] H. Jang, F. Liu, G. Zhao, T. Bradshaw, and A. B. McMillan. Technical note: Deep learning based mrac using rapid ultrashort echo time imaging. *Medical Physics*, 2018. ISSN 0094-2405. doi: 10.1002/mp.12964.

- [57] Xun Jia, Bin Dong, Yifei Lou, and Jiang. Steve B. Gpu-based iterative cone-beam ct reconstruction using tight frame regularization. *Physics in Medicine & Biology*, 56(13):3787, 2011. ISSN 0031-9155. URL <http://stacks.iop.org/0031-9155/56/i=13/a=004>.
- [58] J. Jiang, Y. C. Hu, N. Tyagi, P. Zhang, A. Rimmer, J. O. Deasy, and H. Veeraraghavan. Cross-modality (ct-mri) prior augmented deep learning for robust lung tumor segmentation from small mr datasets. *Medical Physics*, 46(10):4392–4404, 2019. ISSN 0094-2405. doi: 10.1002/mp.13695.
- [59] Cheng-Bin Jin, Hakil Kim, Mingjie Liu, In Ho Han, Jae Il Lee, Jung Hwan Lee, Seongsu Joo, Eunsik Park, Young Saem Ahn, and Xuenan Cui. Dc2anet: Generating lumbar spine mr images from ct scan data based on semi-supervised learning. *Applied Sciences*, 9(12):2521, 2019. ISSN 2076-3417. URL <https://www.mdpi.com/2076-3417/9/12/2521>.
- [60] Cheng-Bin Jin, Hakil Kim, Mingjie Liu, Wonmo Jung, Seongsu Joo, Eunsik Park, Young Saem Ahn, In Ho Han, Jae Il Lee, and Xuenan Cui. Deep ct to mr synthesis using paired and unpaired data. *Sensors*, 19(10):2361, 2019. ISSN 1424-8220. URL <https://www.mdpi.com/1424-8220/19/10/2361>.
- [61] K. H. Jin, M. T. McCann, E. Froustey, and M. Unser. Deep convolutional neural network for inverse problems in imaging. *IEEE Transactions on Image Processing*, 26(9):4509–4522, 2017. ISSN 1941-0042. doi: 10.1109/TIP.2017.2713099.
- [62] P. Jin, C. A. Bouman, and K. D. Sauer. A model-based image reconstruction algorithm with simultaneous beam hardening correction for x-ray ct. *IEEE Transactions on Computational Imaging*, 1(3):200–216, 2015. ISSN 2333-9403. doi: 10.1109/TCI.2015.2461492.
- [63] Adam Johansson, Mikael Karlsson, and Tufve Nyholm. Ct substitute derived from mri sequences with ultrashort echo time. *Medical Physics*, 38(5):2708–2714, 2011. ISSN 2473-4209. doi: 10.1118/1.3578928. URL <http://dx.doi.org/10.1118/1.3578928>.
- [64] E. Johnstone, J. J. Wyatt, A. M. Henry, S. C. Short, D. Sebag-Montefiore, L. Murray, C. G. Kelly, H. M. McCallum, and R. Speight. Systematic review of synthetic computed tomography generation methodologies for use in magnetic resonance imaging-only radiation therapy. *International Journal of Radiation Oncology*Biophysics*Physics*, 100(1):199–217, 2018. ISSN 0360-3016. doi: 10.1016/j.ijrobp.2017.08.043.
- [65] Joakim H. Jonsson, Magnus G. Karlsson, Mikael Karlsson, and Tufve Nyholm. Treatment planning using mri data: an analysis of the dose calculation accuracy for different treatment regions. *Radiation Oncology*, 5(1):62, 2010. ISSN 1748-717X. doi: 10.1186/1748-717x-5-62. URL <https://doi.org/10.1186/1748-717x-5-62>.
- [66] W. A. Kalender, H. Wolf, and C. Suess. Dose reduction in ct by anatomically adapted tube current modulation. ii. phantom measurements. *Medical Physics*, 26(11):2248–53, 1999. ISSN 0094-2405 (Print) 0094-2405. doi: 10.1118/1.598738.
- [67] E. Kang, W. Chang, J. Yoo, and J. C. Ye. Deep convolutional framelet denosing for low-dose ct via wavelet residual network. *IEEE Transactions on Medical Imaging*, 37(6):1358–1369, 2018. ISSN 1558-254X. doi: 10.1109/TMI.2018.2823756.
- [68] Eunhee Kang, Junhong Min, and Jong Chul Ye. A deep convolutional neural network using directional wavelets for low-dose x-ray ct reconstruction. *Medical Physics*, 44(10):e360–e375, 2017. ISSN 0094-2405. doi: 10.1002/mp.12344. URL <https://aapm.onlinelibrary.wiley.com/doi/abs/10.1002/mp.12344>.
- [69] Sydney Kaplan and Yang-Ming Zhu. Full-dose pet image estimation from low-dose pet image using deep learning: a pilot study. *Journal of Digital Imaging*, 32(5):773–778, 2019. ISSN 1618-727X. doi: 10.1007/s10278-018-0150-3. URL <https://doi.org/10.1007/s10278-018-0150-3>.
- [70] S. Kazemifar, S. McGuire, R. Timmerman, Z. Wardak, D. Nguyen, Y. Park, S. Jiang, and A. Owangi. Mri-only brain radiotherapy: Assessing the dosimetric accuracy of synthetic ct images generated using a deep learning approach. *Radiotherapy and Oncology*, 136:56–63, 2019. ISSN 0167-8140. doi: 10.1016/j.radonc.2019.03.026.

- [71] V. S. Khoo and D. L. Joon. New developments in mri for target volume delineation in radiotherapy. *The British Journal of Radiology*, 79 Spec No 1:S2–15, 2006. ISSN 0007-1285. doi: 10.1259/bjr/41321492.
- [72] S. Kida, T. Nakamoto, M. Nakano, K. Nawa, A. Haga, J. Kotoku, H. Yamashita, and K. Nakagawa. Cone beam computed tomography image quality improvement using a deep convolutional neural network. *Cureus*, 10(4):e2548, 2018. ISSN 2168-8184 (Print) 2168-8184. doi: 10.7759/cureus.2548.
- [73] Satoshi Kida, Shizuo Kaji, Kanabu Nawa, Toshikazu Imae, Takahiro Nakamoto, Sho Ozaki, Takeshi Ohta, Yuki Nozawa, and Keiichi Nakagawa. Visual enhancement of cone-beam ct by use of cyclegan. *Medical Physics*, 47(3):998–1010, 2020. ISSN 0094-2405. doi: 10.1002/mp.13963. URL <https://aapm.onlinelibrary.wiley.com/doi/abs/10.1002/mp.13963>.
- [74] K. H. Kim, W. J. Do, and S. H. Park. Improving resolution of mr images with an adversarial network incorporating images with different contrast. *Medical Physics*, 45(7):3120–3131, 2018. ISSN 0094-2405. doi: 10.1002/mp.12945.
- [75] P. E. Kinahan, D. W. Townsend, T. Beyer, and D. Sashin. Attenuation correction for a combined 3d pet/ct scanner. *Medical Physics*, 25(10):2046–53, 1998. ISSN 0094-2405 (Print) 0094-2405. doi: 10.1118/1.598392.
- [76] Y. Koike, Y. Akino, I. Sumida, H. Shiomi, H. Mizuno, M. Yagi, F. Isohashi, Y. Seo, O. Suzuki, and K. Ogawa. Feasibility of synthetic computed tomography generated with an adversarial network for multi-sequence magnetic resonance-based brain radiotherapy. *Journal of Radiation Research*, 61(1):92–103, 2020. ISSN 0449-3060. doi: 10.1093/jrr/rrz063.
- [77] Brian Holch Kristensen, Finn J?rgen Laursen, Vibeke L?gager, Poul Flemming Geertsen, and Anders Krarup-Hansen. Dosimetric and geometric evaluation of an open low-field magnetic resonance simulator for radiotherapy treatment planning of brain tumours. *Radiotherapy and Oncology*, 87(1):100–109, 2008. ISSN 0167-8140. doi: <https://doi.org/10.1016/j.radonc.2008.01.014>. URL <http://www.sciencedirect.com/science/article/pii/S0167814008000431>.
- [78] Christopher Kurz, Matteo Maspero, Mark H. F. Savenije, Guillaume Landry, Florian Kamp, Marco Pinto, Minglun Li, Katia Parodi, Claus Belka, and Cornelis A. T. van den Berg. Cbct correction using a cycle-consistent generative adversarial network and unpaired training to enable photon and proton dose calculation. *Physics in Medicine & Biology*, 64(22):225004, 2019. ISSN 1361-6560. doi: 10.1088/1361-6560/ab4d8c. URL <http://dx.doi.org/10.1088/1361-6560/ab4d8c>.
- [79] Y. Kyriakou, T. Riedel, and W. A. Kalender. Combining deterministic and monte carlo calculations for fast estimation of scatter intensities in ct. *Physics in Medicine & Biology*, 51(18):4567–86, 2006. ISSN 0031-9155 (Print) 0031-9155. doi: 10.1088/0031-9155/51/18/008.
- [80] C. N. Ladefoged, L. Marnier, A. Hindsholm, I. Law, L. Hojgaard, and F. L. Andersen. Deep learning based attenuation correction of pet/mri in pediatric brain tumor patients: Evaluation in a clinical setting. *Frontiers in Neuroscience*, 12:1005, 2018. ISSN 1662-4548 (Print) 1662-453x. doi: 10.3389/fnins.2018.01005.
- [81] Jan J. W. Lagendijk, Bas W. Raaymakers, Alexander J. E. Raaijmakers, Johan Overweg, Kevin J. Brown, Ellen M. Kerkhof, Richard W. van der Put, Bj?rn H?rdemark, Marco van Vulpen, and Uulke A. van der Heide. Mri/linac integration. *Radiotherapy and Oncology*, 86(1):25–29, 2008. ISSN 0167-8140. doi: <https://doi.org/10.1016/j.radonc.2007.10.034>. URL <http://www.sciencedirect.com/science/article/pii/S0167814007005476>.
- [82] Jonathan Lambert, Peter B. Greer, Fred Menk, Jackie Patterson, Joel Parker, Kara Dahl, Sanjiv Gupta, Anne Capp, Chris Wratten, Colin Tang, Mahesh Kumar, Jason Dowling, Sarah Hauville, Cynthia Hughes, Kristen Fisher, Peter Lau, James W. Denham, and Olivier Salvado. Mri-guided prostate radiation therapy planning: Investigation of dosimetric accuracy of mri-based dose planning. *Radiotherapy and Oncology*, 98(3):330–334, 2011. ISSN 0167-8140. doi: <https://doi.org/10.1016/j.radonc.2011.01.012>. URL <http://www.sciencedirect.com/science/article/pii/S0167814011000272>.

- [83] Guillaume Landry, David Hansen, Florian Kamp, Minglun Li, Ben Hoyle, Jochen Weller, Katia Parodi, Claus Belka, and Christopher Kurz. Comparing unet training with three different datasets to correct cbct images for prostate radiotherapy dose calculations. *Physics in Medicine & Biology*, 64(3):035011, 2019. ISSN 1361-6560. doi: 10.1088/1361-6560/aaf496. URL <http://dx.doi.org/10.1088/1361-6560/aaf496>.
- [84] A. Largent, A. Barateau, J. C. Nunes, E. Mylona, J. Castelli, C. Lafond, P. B. Greer, J. A. Dowling, J. Baxter, H. Saint-Jalmes, O. Acosta, and R. de Crevoisier. Comparison of deep learning-based and patch-based methods for pseudo-ct generation in mri-based prostate dose planning. *International Journal of Radiation Oncology*Biophysics*Physics*, 105(5):1137–1150, 2019. ISSN 0360-3016. doi: 10.1016/j.ijrobp.2019.08.049.
- [85] An Le, Zhang Pei, Ehsan Adeli, Wang Yan, Ma Guangkai, Shi Feng, David S. Lalush, Lin Weili, and Shen Dinggang. Multi-level canonical correlation analysis for standard-dose pet image estimation. *IEEE Transactions on Image Processing*, 25(7):3303–3315, 2016. ISSN 1941-0042 1057-7149. doi: 10.1109/TIP.2016.2567072. URL <https://www.ncbi.nlm.nih.gov/pubmed/27187957https://www.ncbi.nlm.nih.gov/pmc/articles/PMC5106345/>.
- [86] H. Lee, J. Lee, H. Kim, B. Cho, and S. Cho. Deep-neural-network-based sinogram synthesis for sparse-view ct image reconstruction. *IEEE Transactions on Radiation and Plasma Medical Sciences*, 3(2):109–119, 2019. ISSN 2469-7303. doi: 10.1109/TRPMS.2018.2867611.
- [87] Jung Hwan Lee, In Ho Han, Dong Hwan Kim, Seunghan Yu, In Sook Lee, You Seon Song, Seongsu Joo, Cheng-Bin Jin, and Hakil Kim. Spine computed tomography to magnetic resonance image synthesis using generative adversarial networks : A preliminary study. *J Korean Neurosurg Soc*, 0, 2020. ISSN 2005-3711. doi: 10.3340/jkns.2019.0084. URL <https://doi.org/10.3340/jkns.2019.0084http://www.jkns.or.kr/journal/view.php?number=7277>.
- [88] Young K. Lee, Marc Bollet, Geoffrey Charles-Edwards, Maggie A. Flower, Martin O. Leach, Helen McNair, Elizabeth Moore, Carl Rowbottom, and Steve Webb. Radiotherapy treatment planning of prostate cancer using magnetic resonance imaging alone. *Radiotherapy and Oncology*, 66(2): 203–216, 2003. ISSN 0167-8140. doi: [https://doi.org/10.1016/S0167-8140\(02\)00440-1](https://doi.org/10.1016/S0167-8140(02)00440-1). URL <http://www.sciencedirect.com/science/article/pii/S0167814002004401>.
- [89] Y. Lei, X. Dong, Tonghe Wang, K. Higgins, T. Liu, W. J. Curran, H. Mao, J. A. Nye, and Xiaofeng Yang. Whole-body pet estimation from low count statistics using cycle-consistent generative adversarial networks. *Physics in Medicine & Biology*, 64(21):215017, 2019. ISSN 0031-9155. doi: 10.1088/1361-6560/ab4891.
- [90] Y. Lei, J. Harms, Tonghe Wang, Y. Liu, H. K. Shu, A. B. Jani, W. J. Curran, H. Mao, T. Liu, and Xiaofeng Yang. Mri-only based synthetic ct generation using dense cycle consistent generative adversarial networks. *Medical Physics*, 46(8):3565–3581, 2019. ISSN 0094-2405. doi: 10.1002/mp.13617.
- [91] Y. Lei, T. Wang, S. Tian, X. Dong, A. B. Jani, D. Schuster, W. J. Curran, P. Patel, T. Liu, and X. Yang. Male pelvic multi-organ segmentation aided by cbct-based synthetic mri. *Physics in Medicine & Biology*, 65(3):035013, 2020. ISSN 0031-9155. doi: 10.1088/1361-6560/ab63bb.
- [92] Yang Lei, Yabo Fu, Hui Mao, Walter Curran, Tian Liu, and Xiaofeng Yang. Multi-modality mri arbitrary transformation using unified generative adversarial networks. In *SPIE Medical Imaging*, volume 11313. SPIE. URL <https://doi.org/10.1117/12.2549794>.
- [93] Yang Lei, Joseph Harms, Tonghe Wang, Yingzi Liu, HuiKuo Shu, Ashesh B Jani, Walter J Curran, Hui Mao, Tian Liu, and Xiaofeng Yang. Mrionly based synthetic ct generation using dense cycle consistent generative adversarial networks. *Medical physics*, 46(8):3565–3581, 2019. ISSN 0094-2405.
- [94] Yang Lei, Xue Dong, Zhen Tian, Yingzi Liu, Sibao Tian, Tonghe Wang, Xiaojun Jiang, Pretesh Patel, Ashesh B. Jani, Hui Mao, Walter J. Curran, Tian Liu, and Xiaofeng Yang. Ct prostate segmentation based on synthetic mri-aided deep attention fully convolution network. *Medical Physics*, 47(2): 530–540, 2020. ISSN 0094-2405. doi: 10.1002/mp.13933. URL <https://aapm.onlinelibrary.wiley.com/doi/abs/10.1002/mp.13933>.

- [95] A. P. Leynes, J. Yang, F. Wiesinger, S. S. Kaushik, D. D. Shanbhag, Y. Seo, T. A. Hope, and P. E. Z. Larson. Zero-echo-time and dixon deep pseudo-ct (zedd ct): Direct generation of pseudo-ct images for pelvic pet/mri attenuation correction using deep convolutional neural networks with multiparametric mri. *Journal of Nuclear Medicine*, 59(5):852–858, 2018. ISSN 0161-5505. doi: 10.2967/jnumed.117.198051.
- [96] B. Li, H. C. Lee, X. Duan, C. Shen, L. Zhou, X. Jia, and M. Yang. Comprehensive analysis of proton range uncertainties related to stopping-power-ratio estimation using dual-energy ct imaging. *Physics in Medicine & Biology*, 62(17):7056–7074, 2017. ISSN 1361-6560. doi: 10.1088/1361-6560/aa7dc9. URL <http://dx.doi.org/10.1088/1361-6560/aa7dc9>.
- [97] Yinghui Li, Jinhan Zhu, Zhibin Liu, Jianjian Teng, Qiuying Xie, Liwen Zhang, Xiaowei Liu, Jinping Shi, and Lixin Chen. A preliminary study of using a deep convolution neural network to generate synthesized ct images based on cbct for adaptive radiotherapy of nasopharyngeal carcinoma. *Physics in Medicine & Biology*, 64(14):145010, 2019. ISSN 1361-6560. doi: 10.1088/1361-6560/ab2770. URL <http://dx.doi.org/10.1088/1361-6560/ab2770>.
- [98] X. Liang, L. Chen, D. Nguyen, Z. Zhou, X. Gu, M. Yang, J. Wang, and S. Jiang. Generating synthesized computed tomography (ct) from cone-beam computed tomography (cbct) using cyclegan for adaptive radiation therapy. *Physics in Medicine & Biology*, 64(12):125002, 2019. ISSN 0031-9155. doi: 10.1088/1361-6560/ab22f9.
- [99] Eugene C. Lin. Radiation risk from medical imaging. *Mayo Clinic Proceedings*, 85(12):1142–1146, 2010. ISSN 0025-6196 1942-5546. doi: 10.4065/mcp.2010.0260. URL <http://www.ncbi.nlm.nih.gov/pmc/articles/PMC2996147/>.
- [100] F. Liu, H. Jang, R. Kijowski, T. Bradshaw, and A. B. McMillan. Deep learning mr imaging-based attenuation correction for pet/mr imaging. *Radiology*, 286(2):676–684, 2018. ISSN 0033-8419. doi: 10.1148/radiol.2017170700.
- [101] F. Liu, H. Jang, R. Kijowski, G. Zhao, T. Bradshaw, and A. B. McMillan. A deep learning approach for (18)f-fdg pet attenuation correction. *EJNMMI physics*, 5(1):24, 2018. ISSN 2197-7364 (Print) 2197-7364. doi: 10.1186/s40658-018-0225-8.
- [102] F. Liu, L. Feng, and R. Kijowski. Mantis: Model-augmented neural network with incoherent k-space sampling for efficient mr parameter mapping. *Magnetic resonance in Medicine*, 82(1):174–188, 2019. ISSN 0740-3194. doi: 10.1002/mrm.27707.
- [103] F. Liu, P. Yadav, A. M. Baschnagel, and A. B. McMillan. Mr-based treatment planning in radiation therapy using a deep learning approach. *Journal of Applied Clinical Medical Physics*, 20(3):105–114, 2019. ISSN 1526-9914. doi: 10.1002/acm2.12554.
- [104] Y. Liu, Y. Lei, T. Wang, O. Kayode, S. Tian, T. Liu, P. Patel, W. J. Curran, L. Ren, and X. Yang. Mri-based treatment planning for liver stereotactic body radiotherapy: validation of a deep learning-based synthetic ct generation method. *The British Journal of Radiology*, 92(1100):20190067, 2019. ISSN 0007-1285. doi: 10.1259/bjr.20190067.
- [105] Y. Liu, Y. Lei, Y. Wang, G. Shafai-Erfani, T. Wang, S. Tian, P. Patel, A. B. Jani, M. McDonald, W. J. Curran, T. Liu, J. Zhou, and X. Yang. Evaluation of a deep learning-based pelvic synthetic ct generation technique for mri-based prostate proton treatment planning. *Physics in Medicine & Biology*, 64(20):205022, 2019. ISSN 0031-9155. doi: 10.1088/1361-6560/ab41af.
- [106] Y. Liu, Y. Lei, Y. Wang, T. Wang, L. Ren, L. Lin, M. McDonald, W. J. Curran, T. Liu, J. Zhou, and X. Yang. Mri-based treatment planning for proton radiotherapy: dosimetric validation of a deep learning-based liver synthetic ct generation method. *Physics in Medicine & Biology*, 64(14):145015, 2019. ISSN 0031-9155. doi: 10.1088/1361-6560/ab25bc.
- [107] Yan Liu and Yi Zhang. Low-dose ct restoration via stacked sparse denoising autoencoders. *Neurocomputing*, 284:80–89, 2018. ISSN 0925-2312. doi: <https://doi.org/10.1016/j.neucom.2018.01.015>. URL <http://www.sciencedirect.com/science/article/pii/S0925231218300316>.

- [108] Yingzi Liu, Yang Lei, Tonghe Wang, Yabo Fu, Xiangyang Tang, Walter J. Curran, Tian Liu, Pretesh Patel, and Xiaofeng Yang. Cbct-based synthetic ct generation using deep-attention cyclegan for pancreatic adaptive radiotherapy. *Medical Physics*, n/a(n/a). ISSN 0094-2405. doi: 10.1002/mp.14121. URL <https://aapm.onlinelibrary.wiley.com/doi/abs/10.1002/mp.14121>.
- [109] B. Lu, H. Lu, and J. Palta. A comprehensive study on decreasing the kilovoltage cone-beam ct dose by reducing the projection number. *Journal of Applied Clinical Medical Physics*, 11(3):3274, 2010. ISSN 1526-9914.
- [110] W. Lu, J. A. Onofrey, Y. Lu, L. Shi, T. Ma, Y. Liu, and C. Liu. An investigation of quantitative accuracy for deep learning based denoising in oncological pet. *Physics in Medicine & Biology*, 64(16):165019, 2019. ISSN 0031-9155. doi: 10.1088/1361-6560/ab3242.
- [111] N. Mail, D. J. Moseley, J. H. Siewerdsen, and D. A. Jaffray. The influence of bowtie filtration on cone-beam ct image quality. *Medical Physics*, 36(1):22–32, 2009. doi: doi:http://dx.doi.org/10.1118/1.3017470. URL <http://scitation.aip.org/content/aapm/journal/medphys/36/1/10.1118/1.3017470>.
- [112] T. E. Marchant, C. J. Moore, C. G. Rowbottom, R. I. MacKay, and P. C. Williams. Shading correction algorithm for improvement of cone-beam ct images in radiotherapy. *Physics in Medicine & Biology*, 53(20):5719, 2008. ISSN 0031-9155. URL <http://stacks.iop.org/0031-9155/53/i=20/a=010>.
- [113] M. Mardani, E. Gong, J. Y. Cheng, S. S. Vasanaawala, G. Zaharchuk, L. Xing, and J. M. Pauly. Deep generative adversarial neural networks for compressive sensing mri. *IEEE Transactions on Medical Imaging*, 38(1):167–179, 2019. ISSN 1558-254X. doi: 10.1109/TMI.2018.2858752.
- [114] M. Maspero, M. H. F. Savenije, A. M. Dinkla, P. R. Seevinck, M. P. W. Intven, I. M. Jurgenliemk-Schulz, L. G. W. Kerkmeijer, and C. A. T. van den Berg. Dose evaluation of fast synthetic-ct generation using a generative adversarial network for general pelvis mr-only radiotherapy. *Physics in Medicine & Biology*, 63(18):185001, 2018. ISSN 0031-9155. doi: 10.1088/1361-6560/aada6d.
- [115] C. H. McCollough, A. C. Bartley, R. E. Carter, B. Chen, T. A. Drees, P. Edwards, 3rd Holmes, D. R., A. E. Huang, F. Khan, S. Leng, K. L. McMillan, G. J. Michalak, K. M. Nunez, L. Yu, and J. G. Fletcher. Low-dose ct for the detection and classification of metastatic liver lesions: Results of the 2016 low dose ct grand challenge. *Medical Physics*, 44(10):e339–e352, 2017. ISSN 0094-2405. doi: 10.1002/mp.12345.
- [116] E. M. McKenzie, A. Santhanam, D. Ruan, D. O’Connor, M. Cao, and K. Sheng. Multimodality image registration in the head-and-neck using a deep learning-derived synthetic ct as a bridge. *Medical Physics*, 2019. ISSN 0094-2405. doi: 10.1002/mp.13976.
- [117] A. D. Missert, L. Yu, S. Leng, J. G. Fletcher, and C. H. McCollough. Synthesizing images from multiple kernels using a deep convolutional neural network. *Medical Physics*, 47(2):422–430, 2020. ISSN 0094-2405. doi: 10.1002/mp.13918.
- [118] S. Neppl, G. Landry, C. Kurz, D. C. Hansen, B. Hoyle, S. Stocklein, M. Seidensticker, J. Weller, C. Belka, K. Parodi, and F. Kamp. Evaluation of proton and photon dose distributions recalculated on 2d and 3d unet-generated pseudocts from t1-weighted mr head scans. *Acta Oncol*, 58(10):1429–1434, 2019. ISSN 0284-186x. doi: 10.1080/0284186x.2019.1630754.
- [119] Patricia K. Nguyen and Joseph C. Wu. Radiation exposure from imaging tests: is there an increased cancer risk? *Expert Review of Cardiovascular Therapy*, 9(2):177–183, 2011. ISSN 1477-9072 1744-8344. doi: 10.1586/erc.10.184. URL <http://www.ncbi.nlm.nih.gov/pmc/articles/PMC3102578/>.
- [120] D. Nie, R. Trullo, J. Lian, L. Wang, C. Petitjean, S. Ruan, Q. Wang, and D. Shen. Medical image synthesis with deep convolutional adversarial networks. *IEEE Transactions on Bio-medical Engineering*, 65(12):2720–2730, 2018. ISSN 0018-9294. doi: 10.1109/tbme.2018.2814538.
- [121] Ruola Ning, Xiangyang Tang, and David Conover. X-ray scatter correction algorithm for cone beam ct imaging. *Medical Physics*, 31(5):1195–1202, 2004. doi: doi:http://dx.doi.org/10.1118/1.1711475. URL <http://scitation.aip.org/content/aapm/journal/medphys/31/5/10.1118/1.1711475>.

- [122] T. Niu and L. Zhu. Accelerated barrier optimization compressed sensing (abocs) reconstruction for cone-beam ct: phantom studies. *Medical Physics*, 39(7):4588–98, 2012. ISSN 0094-2405 (Print) 0094-2405. doi: 10.1118/1.4729837.
- [123] Yusuke Nomura, Qiong Xu, Hiroki Shirato, Shinichi Shimizu, and Lei Xing. Projection-domain scatter correction for cone beam computed tomography using a residual convolutional neural network. *Medical Physics*, 46(7):3142–3155, 2019. ISSN 0094-2405. doi: 10.1002/mp.13583. URL <https://aapm.onlinelibrary.wiley.com/doi/abs/10.1002/mp.13583>.
- [124] Tufve Nyholm, Morgan Nyberg, Magnus G. Karlsson, and Mikael Karlsson. Systematisation of spatial uncertainties for comparison between a mr and a ct-based radiotherapy workflow for prostate treatments. *Radiation Oncology*, 4(1):54, 2009. ISSN 1748-717X. doi: 10.1186/1748-717x-4-54. URL <https://doi.org/10.1186/1748-717X-4-54>.
- [125] S. Olberg, H. Zhang, W. R. Kennedy, J. Chun, V. Rodriguez, I. Zoberi, M. A. Thomas, J. S. Kim, S. Mutic, O. L. Green, and J. C. Park. Synthetic ct reconstruction using a deep spatial pyramid convolutional framework for mr-only breast radiotherapy. *Medical Physics*, 46(9):4135–4147, 2019. ISSN 0094-2405. doi: 10.1002/mp.13716.
- [126] J. Ouyang, K. T. Chen, E. Gong, J. Pauly, and G. Zaharchuk. Ultra-low-dose pet reconstruction using generative adversarial network with feature matching and task-specific perceptual loss. *Medical Physics*, 46(8):3555–3564, 2019. ISSN 0094-2405. doi: 10.1002/mp.13626.
- [127] Atul Padole, Ranish Deedar Ali Khawaja, Mannudeep K. Kalra, and Sarabjeet Singh. Ct radiation dose and iterative reconstruction techniques. *American Journal of Roentgenology*, 204(4):W384–W392, 2015. ISSN 0361-803X. doi: 10.2214/AJR.14.13241. URL <http://dx.doi.org/10.2214/AJR.14.13241>.
- [128] Angela U Pathmanathan, Helen A McNair, Maria A Schmidt, Douglas H Brand, Louise Delacroix, Cynthia L Eccles, Alexandra Gordon, Trina Herbert, Nicholas J van As, Robert A Huddart, and Alison C Tree. Comparison of prostate delineation on multimodality imaging for mr-guided radiotherapy. *The British Journal of Radiology*, 92(1096):20180948, 2019. doi: 10.1259/bjr.20180948. URL <https://www.birpublications.org/doi/abs/10.1259/bjr.20180948>.
- [129] M. Qi, Y. Li, A. Wu, Q. Jia, B. Li, W. Sun, Z. Dai, X. Lu, L. Zhou, X. Deng, and T. Song. Multi-sequence mr image-based synthetic ct generation using a generative adversarial network for head and neck mri-only radiotherapy. *Medical Physics*, 2020. ISSN 0094-2405. doi: 10.1002/mp.14075.
- [130] Liangqiong Qu, Yongqin Zhang, Shuai Wang, Pew-Thian Yap, and Dinggang Shen. Synthesized 7t mri from 3t mri via deep learning in spatial and wavelet domains. *Medical Image Analysis*, 62:101663, 2020. ISSN 1361-8415. doi: <https://doi.org/10.1016/j.media.2020.101663>. URL <http://www.sciencedirect.com/science/article/pii/S1361841520300293>.
- [131] T. M. Quan, T. Nguyen-Duc, and W. Jeong. Compressed sensing mri reconstruction using a generative adversarial network with a cyclic loss. *IEEE Transactions on Medical Imaging*, 37(6):1488–1497, 2018. ISSN 1558-254X. doi: 10.1109/TMI.2018.2820120.
- [132] Zhang Ruoqiao, J. B. Thibault, C. A. Bouman, K. D. Sauer, and Hsieh Jiang. Model-based iterative reconstruction for dual-energy x-ray ct using a joint quadratic likelihood model. *IEEE Transactions on Medical Imaging*, 33(1):117–134, 2014. ISSN 0278-0062. doi: 10.1109/TMI.2013.2282370.
- [133] A. Sanaat, H. Arabi, I. Mainta, V. Garibotto, and H. Zaidi. Projection-space implementation of deep learning-guided low-dose brain pet imaging improves performance over implementation in image-space. *Journal of Nuclear Medicine*, 2020. ISSN 0161-5505. doi: 10.2967/jnumed.119.239327.
- [134] K. G. Schilling, J. Blaber, Y. Huo, A. Newton, C. Hansen, V. Nath, A. T. Shafer, O. Williams, S. M. Resnick, B. Rogers, A. W. Anderson, and B. A. Landman. Synthesized b0 for diffusion distortion correction (synb0-disco). *Magnetic Resonance Imaging*, 64:62–70, 2019. ISSN 0730-725x. doi: 10.1016/j.mri.2019.05.008.

- [135] J. Schlemper, J. Caballero, J. V. Hajnal, A. N. Price, and D. Rueckert. A deep cascade of convolutional neural networks for dynamic mr image reconstruction. *IEEE Transactions on Medical Imaging*, 37(2):491–503, 2018. ISSN 0278-0062. doi: 10.1109/tmi.2017.2760978.
- [136] G. Shafai-Erfani, Y. Lei, Y. Liu, Y. Wang, T. Wang, J. Zhong, T. Liu, M. McDonald, W. J. Curran, J. Zhou, H. K. Shu, and X. Yang. Mri-based proton treatment planning for base of skull tumors. *International Journal of Particle Therapy*, 6(2):12–25, 2019. ISSN 2331-5180. doi: 10.14338/ijpt-19-00062.1.
- [137] H. Shan, Y. Zhang, Q. Yang, U. Kruger, M. K. Kalra, L. Sun, W. Cong, and G. Wang. 3-d convolutional encoder-decoder network for low-dose ct via transfer learning from a 2-d trained network. *IEEE Transactions on Medical Imaging*, 37(6):1522–1534, 2018. ISSN 1558-254X. doi: 10.1109/TMI.2018.2832217.
- [138] Hongming Shan, Atul Padole, Fatemeh Homayounieh, Uwe Kruger, Ruhani Doda Khera, Chayanin Nitiwarangkul, Mannudeep K. Kalra, and Ge Wang. Competitive performance of a modularized deep neural network compared to commercial algorithms for low-dose ct image reconstruction. *Nature Machine Intelligence*, 1(6):269–276, 2019. ISSN 2522-5839. doi: 10.1038/s42256-019-0057-9. URL <https://doi.org/10.1038/s42256-019-0057-9>.
- [139] I. Shiri, P. Ghafarian, P. Geramifar, K. H. Leung, M. Ghelichoghli, M. Oveisi, A. Rahmim, and M. R. Ay. Direct attenuation correction of brain pet images using only emission data via a deep convolutional encoder-decoder (deep-dac). *European Radiology*, 29(12):6867–6879, 2019. ISSN 0938-7994. doi: 10.1007/s00330-019-06229-1.
- [140] J. H. Siewerdsen, D. J. Moseley, B. Bakhtiar, S. Richard, and D. A. Jaffray. The influence of antiscatter grids on soft-tissue detectability in cone-beam computed tomography with flat-panel detectors. *Medical Physics*, 31(12):3506–3520, 2004. doi: doi:http://dx.doi.org/10.1118/1.1819789. URL <http://scitation.aip.org/content/aapm/journal/medphys/31/12/10.1118/1.1819789>.
- [141] Jeffrey H. Siewerdsen and David A. Jaffray. Optimization of x-ray imaging geometry (with specific application to flat-panel cone-beam computed tomography). *Medical Physics*, 27(8):1903–1914, 2000. doi: doi:http://dx.doi.org/10.1118/1.1286590. URL <http://scitation.aip.org/content/aapm/journal/medphys/27/8/10.1118/1.1286590>.
- [142] J. Sjölund, D. Forsberg, M. Andersson, and H. Knutsson. Generating patient specific pseudo-ct of the head from mr using atlas-based regression. *Physics in Medicine & Biology*, 60(2):825, 2015. ISSN 0031-9155. URL <http://stacks.iop.org/0031-9155/60/i=2/a=825>.
- [143] S. J. Son, B. Y. Park, K. Byeon, and H. Park. Synthesizing diffusion tensor imaging from functional mri using fully convolutional networks. *Computers in Biology and Medicine*, 115:103528, 2019. ISSN 0010-4825. doi: 10.1016/j.combiomed.2019.103528.
- [144] K. D. Spuhler, 3rd Gardus, J., Y. Gao, C. DeLorenzo, R. Parsey, and C. Huang. Synthesis of patient-specific transmission data for pet attenuation correction for pet/mri neuroimaging using a convolutional neural network. *Journal of Nuclear Medicine*, 60(4):555–560, 2019. ISSN 0161-5505. doi: 10.2967/jnumed.118.214320.
- [145] Z. Tian, X. Jia, K. Yuan, T. Pan, and S. B. Jiang. Low-dose ct reconstruction via edge-preserving total variation regularization. *Physics in Medicine & Biology*, 56(18):5949–67, 2011. ISSN 0031-9155. doi: 10.1088/0031-9155/56/18/011.
- [146] X. Tie, S. K. Lam, Y. Zhang, K. H. Lee, K. H. Au, and J. Cai. Pseudo-ct generation from multi-parametric mri using a novel multi-channel multi-path conditional generative adversarial network for nasopharyngeal carcinoma patients. *Medical Physics*, 2020. ISSN 0094-2405. doi: 10.1002/mp.14062.
- [147] A. Torrado-Carvajal, J. Vera-Olmos, D. Izquierdo-Garcia, O. A. Catalano, M. A. Morales, J. Margolin, A. Soricelli, M. Salvatore, N. Malpica, and C. Catana. Dixon-vibe deep learning (divide) pseudo-ct synthesis for pelvis pet/mr attenuation correction. *Journal of Nuclear Medicine*, 60(3):429–435, 2019. ISSN 0161-5505. doi: 10.2967/jnumed.118.209288.

- [148] J. Uh, T. E. Merchant, Y. Li, X. Li, and C. Hua. Mri-based treatment planning with pseudo ct generated through atlas registration. *Medical Physics*, 41(5):051711, 2014. ISSN 0094-2405. doi: 10.1118/1.4873315.
- [149] Kenneth Ulin, Marcia M. Urie, and Joel M. Cherlow. Results of a multi-institutional benchmark test for cranial ct/mr image registration. *International Journal of Radiation Oncology*Biophysics*, 77(5):1584–1589, 2010. ISSN 0360-3016. doi: <https://doi.org/10.1016/j.ijrobp.2009.10.017>. URL <http://www.sciencedirect.com/science/article/pii/S036030160903404X>.
- [150] U. A. van der Heide, A. C. Houweling, G. Groenendaal, R. G. Beets-Tan, and P. Lambin. Functional mri for radiotherapy dose painting. *Magnetic Resonance Imaging*, 30(9):1216–23, 2012. ISSN 0730-725x. doi: 10.1016/j.mri.2012.04.010.
- [151] G. M. Villeirs, K. Van Vaerenbergh, L. Vakaet, S. Bral, F. Claus, W. J. De Neve, K. L. Verstraete, and G. O. De Meerleer. Interobserver delineation variation using ct versus combined ct + mri in intensity-modulated radiotherapy for prostate cancer. *Strahlenther Onkol*, 181(7):424–30, 2005. ISSN 0179-7158 (Print) 0179-7158. doi: 10.1007/s00066-005-1383-x.
- [152] T. Wang, Y. Lei, Z. Tian, X. Dong, Y. Liu, X. Jiang, W. J. Curran, T. Liu, H. K. Shu, and X. Yang. Deep learning-based image quality improvement for low-dose computed tomography simulation in radiation therapy. *Journal of Medical Imaging*, 6(4):043504, 2019. ISSN 2329-4302 (Print) 2329-4302. doi: 10.1117/1.jmi.6.4.043504.
- [153] Tonghe Wang and Lei Zhu. Dual energy ct with one full scan and a second sparse-view scan using structure preserving iterative reconstruction (spir). *Physics in Medicine & Biology*, 61(18):6684, 2016. ISSN 0031-9155. URL <http://stacks.iop.org/0031-9155/61/i=18/a=6684>.
- [154] Tonghe Wang and Lei Zhu. Pixel-wise estimation of noise statistics on iterative ct reconstruction from a single scan. *Medical Physics*, 44(7):3525–3533, 2017. ISSN 2473-4209. doi: 10.1002/mp.12302. URL <http://dx.doi.org/10.1002/mp.12302>.
- [155] Tonghe Wang, Yang Lei, Nivedh Manohar, Sibotian, Ashesh B Jani, Hui-Kuo Shu, Kristin Higgins, Anees Dhabaan, Pretesh Patel, and Xiangyang Tang. Dosimetric study on learning-based cone-beam ct correction in adaptive radiation therapy. *Medical Dosimetry*, 44(4):e71–e79, 2019. ISSN 0958-3947.
- [156] Tonghe Wang, Nivedh Manohar, Yang Lei, Anees Dhabaan, Hui-Kuo Shu, Tian Liu, Walter J. Curran, and Xiaofeng Yang. Mri-based treatment planning for brain stereotactic radiosurgery: Dosimetric validation of a learning-based pseudo-ct generation method. *Medical Dosimetry*, 44(3):199–204, 2019. ISSN 0958-3947. doi: <https://doi.org/10.1016/j.meddos.2018.06.008>. URL <http://www.sciencedirect.com/science/article/pii/S0958394718300888>.
- [157] Y. Wang, B. Yu, L. Wang, C. Zu, D. S. Lalush, W. Lin, X. Wu, J. Zhou, D. Shen, and L. Zhou. 3d conditional generative adversarial networks for high-quality pet image estimation at low dose. *Neuroimage*, 174:550–562, 2018. ISSN 1053-8119. doi: 10.1016/j.neuroimage.2018.03.045.
- [158] Y. Wang, C. Liu, X. Zhang, and W. Deng. Synthetic ct generation based on t2 weighted mri of nasopharyngeal carcinoma (npc) using a deep convolutional neural network (dcnn). *Frontiers in Oncology*, 9:1333, 2019. ISSN 2234-943X (Print) 2234-943x. doi: 10.3389/fonc.2019.01333.
- [159] Y. Wang, L. Zhou, B. Yu, L. Wang, C. Zu, D. S. Lalush, W. Lin, X. Wu, J. Zhou, and D. Shen. 3d auto-context-based locality adaptive multi-modality gans for pet synthesis. *IEEE Transactions on Medical Imaging*, 38(6):1328–1339, 2019. ISSN 0278-0062. doi: 10.1109/tmi.2018.2884053.
- [160] Y. Wang, L. Zhou, L. Wang, B. Yu, C. Zu, D. S. Lalush, W. Lin, X. Wu, J. Zhou, and D. Shen. Locality adaptive multi-modality gans for high-quality pet image synthesis. In *Med Image Comput Comput Assist Interv*, volume 11070, pages 329–337, PMC6494468. doi: 10.1007/978-3-030-00928-1_38.
- [161] W. Wei, E. Poirion, B. Bodini, S. Durrleman, O. Colliot, B. Stankoff, and N. Ayache. Fluid-attenuated inversion recovery mri synthesis from multisequence mri using three-dimensional fully convolutional networks for multiple sclerosis. *Journal of Medical Imaging*, 6(1):014005, 2019. ISSN 2329-4302 (Print) 2329-4302. doi: 10.1117/1.jmi.6.1.014005.

- [162] J. M. Wolterink, T. Leiner, M. A. Viergever, and I. Išgum. Generative adversarial networks for noise reduction in low-dose ct. *IEEE Transactions on Medical Imaging*, 36(12):2536–2545, 2017. ISSN 1558-254X. doi: 10.1109/TMI.2017.2708987.
- [163] Y. Wu, Y. Ma, D. P. Capaldi, J. Liu, W. Zhao, J. Du, and L. Xing. Incorporating prior knowledge via volumetric deep residual network to optimize the reconstruction of sparsely sampled mri. *Magnetic Resonance Imaging*, 66:93–103, 2020. ISSN 0730-725x. doi: 10.1016/j.mri.2019.03.012.
- [164] L. Xiang, Y. Qiao, D. Nie, L. An, Q. Wang, and D. Shen. Deep auto-context convolutional neural networks for standard-dose pet image estimation from low-dose pet/mri. *Neurocomputing*, 267: 406–416, 2017. ISSN 0925-2312 (Print) 0925-2312. doi: 10.1016/j.neucom.2017.06.048.
- [165] Lei Xiang, Qian Wang, Dong Nie, Lichi Zhang, Xiyao Jin, Yu Qiao, and Dinggang Shen. Deep embedding convolutional neural network for synthesizing ct image from t1-weighted mr image. *Medical Image Analysis*, 47:31–44, 2018. ISSN 1361-8415. doi: <https://doi.org/10.1016/j.media.2018.03.011>. URL <http://www.sciencedirect.com/science/article/pii/S1361841518301257>.
- [166] S. Xie, C. Yang, Z. Zhang, and H. Li. Scatter artifacts removal using learning-based method for cbct in igr system. *IEEE Access*, 6:78031–78037, 2018. ISSN 2169-3536. doi: 10.1109/ACCESS.2018.2884704.
- [167] J. Yang, D. Park, G. T. Gullberg, and Y. Seo. Joint correction of attenuation and scatter in image space using deep convolutional neural networks for dedicated brain (18)f-fdg pet. *Physics in Medicine & Biology*, 64(7):075019, 2019. ISSN 0031-9155. doi: 10.1088/1361-6560/ab0606.
- [168] Q. Yang, P. Yan, Y. Zhang, H. Yu, Y. Shi, X. Mou, M. K. Kalra, Y. Zhang, L. Sun, and G. Wang. Low-dose ct image denoising using a generative adversarial network with wasserstein distance and perceptual loss. *IEEE Transactions on Medical Imaging*, 37(6):1348–1357, 2018. ISSN 1558-254X. doi: 10.1109/TMI.2018.2827462.
- [169] W. Yang, H. Zhang, J. Yang, J. Wu, X. Yin, Y. Chen, H. Shu, L. Luo, G. Coatrieux, Z. Gui, and Q. Feng. Improving low-dose ct image using residual convolutional network. *IEEE Access*, 5: 24698–24705, 2017. ISSN 2169-3536. doi: 10.1109/ACCESS.2017.2766438.
- [170] Xiaofeng Yang and Baowei Fei. Multiscale segmentation of the skull in mr images for mri-based attenuation correction of combined mr/pet. *Journal of the American Medical Informatics Association*, 20(6):1037–1045, 2013. ISSN 1067-5027. doi: 10.1136/amiajnl-2012-001544. URL <https://doi.org/10.1136/amiajnl-2012-001544>.
- [171] Xiaofeng Yang, Yang Lei, Hui-Kuo Shu, Peter Rossi, Hui Mao, Hyunsuk Shim, Walter J Curran, and Tian Liu. Pseudo ct estimation from mri using patch-based random forest. In *Medical Imaging 2017: Image Processing*, volume 10133, page 101332Q. International Society for Optics and Photonics.
- [172] Xiaofeng Yang, Shengyong Wu, Ioannis Sechopoulos, and Baowei Fei. Cupping artifact correction and automated classification for high-resolution dedicated breast ct images. *Medical Physics*, 39(10):6397–6406, 2012. ISSN 0094-2405. doi: 10.1118/1.4754654. URL <https://aapm.onlinelibrary.wiley.com/doi/abs/10.1118/1.4754654>.
- [173] Xiaofeng Yang, Ning Wu, Guanghui Cheng, Zhengyang Zhou, S Yu David, Jonathan J Beitler, Walter J Curran, and Tian Liu. Automated segmentation of the parotid gland based on atlas registration and machine learning: a longitudinal mri study in head-and-neck radiation therapy. *International Journal of Radiation Oncology* Biology* Physics*, 90(5):1225–1233, 2014. ISSN 0360-3016.
- [174] Xiaofeng Yang, Tonghe Wang, Yang Lei, Kristin Higgins, Tian Liu, Hyunsuk Shim, Walter J Curran, Hui Mao, and Jonathon A Nye. Mri-based attenuation correction for brain pet/mri based on anatomic signature and machine learning. *Physics in Medicine & Biology*, 64(2):025001, 2019. ISSN 0031-9155.
- [175] Xin Yi and Paul Babyn. Sharpness-aware low-dose ct denoising using conditional generative adversarial network. *Journal of Digital Imaging*, 31(5):655–669, 2018. ISSN 1618-727X. doi: 10.1007/s10278-018-0056-0. URL <https://doi.org/10.1007/s10278-018-0056-0>.

- [176] C. You, Q. Yang, H. Shan, L. Gjestebj, G. Li, S. Ju, Z. Zhang, Z. Zhao, Y. Zhang, W. Cong, and G. Wang. Structurally-sensitive multi-scale deep neural network for low-dose ct denoising. *IEEE Access*, 6:41839–41855, 2018. ISSN 2169-3536. doi: 10.1109/ACCESS.2018.2858196.
- [177] B. Yu, Y. Wang, L. Wang, D. Shen, and L. Zhou. Medical image synthesis via deep learning. *Advances in Experimental Medicine and Biology*, 1213:23–44, 2020. ISSN 0065-2598 (Print) 0065-2598. doi: 10.1007/978-3-030-33128-3_2.
- [178] Lifeng Yu, Xin Liu, Shuai Leng, James M. Kofler, Juan C. Ramirez-Giraldo, Mingliang Qu, Jodie Christner, Joel G. Fletcher, and Cynthia H. McCollough. Radiation dose reduction in computed tomography: techniques and future perspective. *Imaging In Medicine*, 1(1):65–84, 2009. ISSN 1755-5191 1755-5205. doi: 10.2217/iim.09.5. URL <http://www.ncbi.nlm.nih.gov/pmc/articles/PMC3271708/>.
- [179] Nimu Yuan, Brandon Dyer, Shyam Rao, Quan Chen, Stanley Benedict, Lu Shang, Yan Kang, Jinyi Qi, and Yi Rong. Convolutional neural network enhancement of fast-scan low-dose cone-beam ct images for head and neck radiotherapy. *Physics in Medicine & Biology*, 65(3):035003, 2020. ISSN 1361-6560. doi: 10.1088/1361-6560/ab6240. URL <http://dx.doi.org/10.1088/1361-6560/ab6240>.
- [180] Y. Zhang, P. T. Yap, L. Qu, J. Z. Cheng, and D. Shen. Dual-domain convolutional neural networks for improving structural information in 3t mri. *Magnetic Resonance Imaging*, 64:90–100, 2019. ISSN 0730-725x. doi: 10.1016/j.mri.2019.05.023.
- [181] T. Zhao, M. McNitt-Gray, and D. Ruan. A convolutional neural network for ultra-low-dose ct denoising and emphysema screening. *Medical Physics*, 46(9):3941–3950, 2019. ISSN 0094-2405. doi: 10.1002/mp.13666.
- [182] Wei Zhao, Kai Niu, Sebastian Schafer, and Kevin Royalty. An indirect transmission measurement-based spectrum estimation method for computed tomography. *Physics in Medicine & Biology*, 60(1):339–357, 2014. ISSN 0031-9155 1361-6560. doi: 10.1088/0031-9155/60/1/339. URL <http://dx.doi.org/10.1088/0031-9155/60/1/339>.
- [183] L. Zhu, N. R. Bennett, and R. Fahrig. Scatter correction method for x-ray ct using primary modulation: theory and preliminary results. *IEEE Transactions on Medical Imaging*, 25(12):1573–87, 2006. ISSN 0278-0062 (Print) 0278-0062.
- [184] Lei Zhu, Yaoqin Xie, Jing Wang, and Lei Xing. Scatter correction for cone-beam ct in radiation therapy. *Medical Physics*, 36(6):2258–2268, 2009. doi: doi:http://dx.doi.org/10.1118/1.3130047. URL <http://scitation.aip.org/content/aapm/journal/medphys/36/6/10.1118/1.3130047>.